ULTRAVIOLET EMITTERS GROWN BY METALORGANIC CHEMICAL VAPOR DEPOSITION

A Thesis
Presented to
The Academic Faculty

by

Yuh-Shiuan Liu

In Partial Fulfillment
of the Requirements for the Degree
Master of Science in the
School of Electrical and Computer Engineering

Georgia Institute of Technology
December 2013

ULTRAVIOLET EMITTERS GROWN BY METALORGANIC CHEMICAL VAPOR DEPOSITION

Approved by:

Professor Russell D. Dupuis, Advisor
School of Electrical and Computer Engineering
Georgia Institute of Technology

Professor Thomas K. Gaylord
School of Electrical and Computer Engineering
Georgia Institute of Technology

Professor P. Douglas Yoder
School of Electrical and Computer Engineering
Georgia Institute of Technology

Date Approved: 18 November 2013

To my parents and my brother

ACKNOWLEDGEMENTS

I am heartily thankful to my advisor, Professor Russell D. Dupuis, for his direction, enthusiasm, encouragement, and all the support starting from the first day I joined Advanced Materials and Devices Group (AMDG). He provided experience and resources that are incomparable with any other academic laboratories in the world. I joined AMDG and learned how to grow III–V materials by MOCVD in his lab which is the best decision I ever made.

I'm very thankful to Dr. Theeradetch Detchprohm for being a wonderful research engineer in our lab. He shared his expensive expertise on MOCVD, bringing a positive attitude on solving research problems, and working closely with me on all the system maintenance. I would like to point out my appreciation to Professor Jae–Hyun Ryou who used to work as a research engineer in our lab. Although I only got to work with Dr. Ryou for few weeks, his preliminary studies have made numerous impacts on work presented in this thesis. In addition, he was very generous on providing guidelines and keeping a good relationship with everyone in the lab even though he is not a research engineer in our lab anymore.

Thanks also goes to all my colleagues in AMDG, notably Dr. Zachary Lochner, my senior mentor who taught me how to operate our A1 reactor growing AlN related material. Although I only get to work with him for a year, he has been a wonderful mentor and friend. Jeomoh Kim, who is always very generous in sharing his knowledge and his research work with me has provided me with a bigger picture of III–N devices.

I would like to extend my appreciations to my colleagues in the Semiconductor Research Laboratory, Computational Electronics and Photonics Group, and Prof.

Ponce's Group at Arizona State University. I especially want to thank Prof. Shyh-Chiang Shen, Prof. P. Douglas Yoder, and Prof. Fernando A. Ponce for leading their group in developing fabrication processes, simulations for the UV–laser diode design, and material characterizations, respectively. I would like to give my special thanks to Tsung–Ting (Louis) Kao and Md. Mahbub Satter for being wonderful team players and wonderful friends; especially, to Louis who spent his valuable time training me on fabrication skills and assisting in growth optimization.

I am grateful to Prof. P. Douglas Yoder and Prof. Thomas K. Gaylord for kindly agreeing to serve on my reading committee. The support of this work by the Microsystem Technology Office (MTO) of the Defense Advanced Research Projects Agency (DARPA) under the Compact Mid-Ultraviolet Technology (CMUVT) program is gratefully acknowledged. In addition, I would like to acknowledge the generous support of the Steve W. Chaddick Endowed Fellowship in Electro-Optics at the Georgia Institute of Technology.

Lastly, I would like to express my loving gratitude to my family. My parents, Nai–Ming Liu and Di–Fang Shyng, who gave me all the possible support to complete my goals. Their encouragement and advice are invaluable to me; especially, they taught me the correct attitude in facing all the problems and challenges which is the main driving force for me to complete this work. I am very grateful to my younger brother, Yuh–Chen Liu, for taking care my parents while I was not around. I'm always proud of him.

TABLE OF CONTENTS

LIST OF TABLES

LIST OF FIGURES

SUMMARY

This thesis presents the development of III–nitride materials for deep–ultraviolet (DUV) light emitting devices. The goal of this research is to develop a DUV laser diode (LD) operating at room temperature. Epitaxial structures for these devices are grown by metalorganic chemical vapor deposition (MOCVD) and several material analysis techniques were employed to characterize these structures such as atomic force microscopy, electroluminescence, Hall–effect measurement, photoluminescence, secondary ion mass spectrometry, transmission electron microscopy, transmission line measurement, and X–ray diffraction. Each of these will be discussed in detail.

The active regions of III–nitride based UV emitters are composed of $Al_xGa_{1-x}N$ alloys, the bandgap of which can be tuned from 3.4 eV to 6.2 eV, which allows us to attain the desired wavelength in the DUV by engineering the molar fraction of aluminum and gallium. In order to emit photons in the DUV wavelength range (> 4.1 eV), high aluminum molar fraction $Al_xGa_{1-x}N$ alloys are required. Since aluminum has very low ad-atom mobility on the growth surface, a very low group V to group III precursor ratio (known as V/III ratio), high growth temperature, and low growth pressure is required to form a smooth surface and subsequently abrupt heterointerfaces. The first part of this work focuses on developing high–quality multi-quantum well structures using high aluminum molar fraction ([Al] $> 60\%$) $Al_xGa_{1-x}N$ alloys. Optically pumped DUV lasers were demonstrated with threshold power density as low as 250 kW/cm^2 for the emission wavelength as short as 248.3 nm. Transverse electric (TE) –like emission dominates when the lasers were operating above threshold power density, which suggests the diode design requires the active region to be fully strained to promote better confinement of the optical mode in transverse direction.

The second phase of this project is to achieve an electrically driven injection diode laser. Owing to their large bandgap, low intrinsic carrier concentration, and relatively high dopant activation energy, the nature of these high aluminum molar fraction materials are highly insulating; therefore, efficiently transport carriers into active region is one of the main challenges. Highly conducting p–type material is especially difficult to achieve because the activation energy for magnesium, a typical dopant, is relatively large and some of the acceptors are compensated by the hydrogen during the growth. Furthermore, due to the lack of a large work function material to form a p–type ohmic contact, the p–contact layer design is limited to low aluminum molar fraction material or gallium nitride. Besides the fabrication challenges, these low aluminum molar fraction materials are not transparent to the laser wavelength causing relatively high internal loss (α_i). In this work, an inverse tapered p–waveguide design is employed to transport holes to active region efficiently while the graded–index separate–confinement heterostructure (GRINSCH) is employed for the active region design. Together, a multi-quantum well (MQW) ultraviolet emitter was demonstrated.

CHAPTER I

INTRODUCTION

Light Amplification by Stimulated Emission of Radiation or "LASER" was first introduced by Gordon Gould at Columbia University in 1959. This invention was then soon applied to semiconductor materials and formed laser diodes (LDs) in 1962 [1–4]. Notably, Nick Holonyak, Jr. of General Electric was the first and only group in 1962 demonstrating "visible" red LD using $GaAs_{1-x}P_x$ ternary alloys [3]. As the III–V material technology advanced, Shuji Nakamura demonstrated the first blue LD in 1996 with the GaN based material system [5]. The breakthrough of Group III–nitride material technology enables more possibilities in fabricating optical emitters outputting wavelength from 200 nm to 1772 nm by alloying InN, GaN, and AlN as shown in Fig.1.

Recently, researchers found interest in deep–UV spectral range (200 – 300 nm) for applications in detection, identification, and decontamination of biological and chemical agents. Currently available mature UV laser systems employ excimer lasers and the frequency mixing of solid state lasers. However, both types of systems are extremely bulky, fragile, and expensive which limits the usage to within a laboratory. With high aluminum composition III–N material, emitting photons in the middle UV spectral region can be realized owing to their nature of direct– and wide–bandgap structure. This thesis will present the development of $Al_xGa_{1-x}N$ materials growth for DUV emitters operating at room temperature.

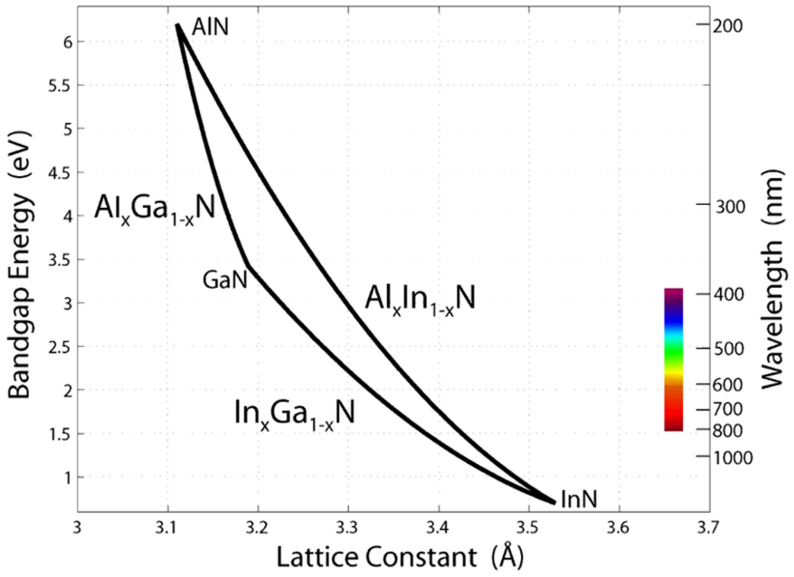

Figure 1: Bandgap energy vs. lattice constant for III–nitride materials.

1.1 III–Nitride Material System

In III–nitride family, i.e., AlN, GaN, InN, and their single crystal alloys exist in three different structures: wurtzite, zinc–blende, and rocksalt [6]. The bulk form of these binary compounds are thermodynamically stable in the wurtzite structure, which is optically anisotropic due to the difference in lattice parameters in different directions. Recently, researchers also reported growth for metastable the zinc–blende structure [7], which is extremely important for optical devices due to the absence of internal electric fields. This crystal structure can lead to larger optical gain and therefore lower laser threshold current density. Figure 2 shows the unit cells for both wurtzite and and zinc–blende cubic structures. In the case of hexagonal/wurtzite crystal structures, they have 120° rotational symmetry; especially, the hexagonal structure has six–fold symmetry along the c–axis. As a result, the four–axes Miller–Bravais indices in form of *(hkil)* is introduced for this crystal structure. Indices *(hki)*

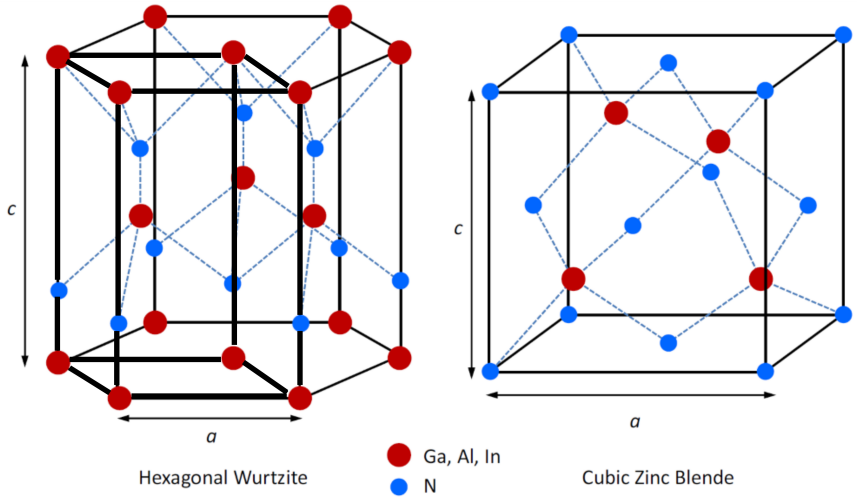

Figure 2: Unit cell of a hexagonal wurtzite structure (left) and a zinc–blende structure (right).

correspond to the three–axes on the basal plane which are 120° apart in the vector direction and *(l)* corresponds to the c axis. Since the *(hki)* are 120° apart from each other, the relationship between the indices can be express as linear superposition: i = -*(h+k)*. On the other hand, the crystal directions in zinc–blende structure are given by [xyz] are numerically equivalent to the Miller indices of the perpendicular planes.

In an ideal wurtzite structure, the ratio for c/a is 8/3; however, the ratios for AlN, GaN, and InN are 1.601, 1.627, and 1.612, respectively. The deviations from the ideal structure originate from the electronegativity difference between the Group III and Group V atoms when they bond to one another. A dipole is generated based on the differences in electronegativity, and results in a polarization charge which significantly alters the device performance in both optical and electrical properties.

All the wurtzite III–nitride binary compounds are direct–bandgap materials. The bandgap energy for each III-nitride binary compound is 0.78 eV, 3.4 eV, and 6.23 eV at room temperature for InN, GaN, and AlN, respectively. In order to produce deep–UV optical emitters, AlN, InN, and GaN can be alloyed to form AlGaN or InAlN

ternary alloys. The bandgap energy (E_g) and the lattice constant (a_0) of the nitride ternary alloys can be formulated by Vegard's Law as:

$$E_g(A_xB_{1-x}N) = xE_g(AN) + (1-x)E_g(BN) - x(1-x)b \tag{1}$$

$$a_0(A_xB_{1-x}N) = xa_0(AN) + (1-x)a_0(BN) \tag{2}$$

where x is an alloy composition ($0 \leq x \leq 1$), b is known as the bowing parameter, and A and B corresponds to group III element. The widely accepted bowing parameters for AlGaN, InGaN, InAlN are 0.7 eV, 1.4 eV, and 3.0 eV, respectively [8–12].

In this study, all the wafers are grown on either AlN native substrates or AlN buffer on sapphire substrates; thus, the biaxial strain effect in the material becomes important as it changes the device band structure and induces a piezoelectric polarization field [13–15]. The in–plane strain elements can be described as:

$$\epsilon = \epsilon_{xx} = \epsilon_{yy} = \frac{a_0 - a(x)}{a_0} \tag{3}$$

where a_0 is the lattice constant of substrate and $a(x)$ is the lattice constant for each epitaxial layer. The strain in the perpendicular direction can be written as:

$$\epsilon_{\perp} = \epsilon_{zz} = -\frac{1}{\nu}\frac{C_{13}}{C_{33}}\epsilon_{xx} \tag{4}$$

where ν is Poisson's ratio and C_{ij}'s are the elastic stiffness constants, which can be obtained based on Vegard's law for ternary alloys. The strain induced shifts in the conduction band can be modeled as

$$\delta E_c = a_{cz}\epsilon_{zz} + a_{ct}(\epsilon_{xx} + \epsilon_{yy}) \tag{5}$$

where a_{cz} and a_{ct} are the hydrostatic deformation potentials for conduction band in perpendicular and tangential direction, respectively. On the other hand, the shift in

Table 1: Physical parameters of III–nitride semiconductors [16, 17].

	GaN	AlN	InN
Lattice Constant, a (Å)	3.189	3.112	3.545
Lattice Constant, c (Å)	5.185	4.982	5.76
Bandgap (eV)	3.39	6.23	0.78
Index of Refraction at 3 eV	2.9	2.15	3.05
Thermal Conductivity, κ (W/cm–K)	1.3	2.0	0.8
Relative Permittivity, ϵ_r	9.5	8.5	15
a_1 (eV)	-4.9	-3.4	-3.5
a_2 (eV)	-11.3	-11.8	-3.5
D_1 (eV)	-3.7	-17.1	-3.7
D_2 (eV)	4.5	7.9	4.5
D_3 (eV)	8.2	8.8	8.2
D_4 (eV)	-4.1	-3.9	-4.1
C_{11} (GPa)	390	396	223
C_{12} (GPa)	145	137	115
C_{13} (GPa)	106	108	92
C_{33} (GPa)	398	373	224
C_{44} (GPa)	105	116	48

valence band is described as

$$\delta E_v = (D_1 + D_3)\epsilon_{zz} + (D_2 + D_4)(\epsilon_{xx} + \epsilon_{yy}) \tag{6}$$

D_1 and D_2 are the hydrostatic deformation potential in valence band while D_3 and D_4 play the role of shear deformation potential in valence band. The relationships between

$$a_1 = a_{cz} - D_1 \qquad a_2 = a_{ct} - D_2 \tag{7}$$

are due to the anisotropic hexagonal structure. Table 1 [16, 17] summarizes various physical parameters of the III–nitride binary materials.

1.2 Metalorganic Chemical Vapor Deposition

Metalorganic Chemical Vapor Deposition (MOCVD) was first introduced by Manasevit [18] at North American Rockwell in 1968. This material growth technology is also known as organometallic chemical vapor deposition (OMCVD), metalorganic vapor phase epitaxy (MOVPE), and organometallic vapor phase epitaxy (OMVPE). The development of this technology was stimulated by the limitations of the state–of–the–art (at the time) liquid phase epitaxy (LPE) growth technology in 1970's. Since the era of LPE, molecular beam epitaxy (MBE), which is introduced by Cho [19], and MOCVD have dominated the research, development, and manufacture of compound semiconductor devices.

In the early development of MOCVD, Manasevit demonstrated the growth of various materials, including GaAs, GaP, AlGaAs, AlN, and GaN [20]. Later, Dupuis, et al. demonstrated some practical devices grown by MOCVD such as, AlGaAs/GaAs solar cells in 1977 [21] and room–temperature operation laser diode in 1978 [22]. MOCVD is the epitaxial crystal growth technology of choice for an impressive array of commercial devices for instance, lasers, light emitting diodes (LEDs), avalanche

photodiodes (APDs), heterojunction bipolar transistors (HBTs), high electron mobility transistors (HEMTs), and solar cells. Virtually every III–V compound semiconductor material system has been grown successfully by MOCVD. Thousands of MOCVD reactors have been sold worldwide, and reactors capable of growing on 69–2 inch wafers or 19–4 inch wafers *in a SINGLE growth run* are commercially available.

An MOCVD process for depositing compound semiconductors is governed by the chemical equation:

$$R_nA + DH_n \rightarrow AD + nRH \tag{8}$$

where R is an organic radical, such as a methyl– or ethyl–radical, and A and D are constituent species for the deposited solid. An example for III–nitride material is give by

$$(CH_3)_3Ga + NH_3 \rightarrow GaN + 3CH_4 \tag{9}$$

A large number of metalorganic (MO) precursors used in MOCVD growth have been studied and Tab.2 shows the commonly used MO sources for III–nitride material growth. During the growth, a molar flow rate of a MO source depends on the flow rate of carrier gas, the pressure of the bubbler (MO source container), and the equilibrium vapor pressure of the precursor. Under thermal equilibrium, the vapor pressure of a MO source can be described with constant A and B in Tab.2 as

$$\log p \text{ (mmHg)} = B - A/T \tag{10}$$

In the case of most commonly used p–type dopant, bis(cyclopentadienyl)magnesium (Cp_2Mg), the vapor pressure equation is revised as

$$\log p \text{ (mmHg)} = B - A/T + 2.18\log T \tag{11}$$

The vapor pressure of these MO sources are highly sensitive to temperature as described by Eq.10 and 11; thus, the bubblers are usually stored in an isothermal water bath to maintain a constant temperature. Metalorganic precursors are transported to

Table 2: Commonly used metalorganic sources in III–nitride material growth.

Metalorganic Compound	Chemical Formula	Molar Mass	Vapor Pressure Constants	
			A	B
Trimethylgallium (TMGa)	$(CH_3)_3Ga$	114.83	1703	8.07
Trimethylaluminum (TMAl)	$(CH_3)_3Al$	72.09	2134.83	8.224
Trimethylindium (TMIn)	$(CH_3)_3In$	159.93	3014	10.52
Bis(cyclopentadienyl) magnesium (Cp_2Mg)	$(C_5H_5)_2Mg$	154.49	4198	25.14

the growth chamber with inert carrier gases, e.g., H_2 or N_2, and the choice of carrier gas depends on the material of interest. Lastly, maintaining the constant total pressure within the bubbler is also critical for maintaining constant bubbling efficiency as the molar flow rate of a MO source can be formulated as

$$Q = \frac{p_{mo}(T)}{p - p_{mo}(T)} \frac{F_{cg}}{C_{STP}} \tag{12}$$

where p is the bubbler pressure, $p_{mo}(T)$ is the equilibrium vapor pressure of the metalorganic source at a given temperature, F_{cg} represnts the flow rate of carrier gas in standard cubic centimeter per minute (sccm), and C_{STP} is 22,406 cc/mole, which is the molar volume of an ideal gas at room temperature and atmosphere pressure. Besides metalorganic precursors, hydrides are also commonly used as n-type dopants and group V precursors. In III-nitride material growth, silane (SiH_4) and ammonia (NH_3) are the most commonly used precursors for n-type dopant and group V precursor, respectively.

An MOCVD reactor consist of three major components: gas delivery system,

growth chamber, and safety infrastructure. Figure 3 shows a simplified schematic diagram for a vertical gas injection MOCVD system. The vertical close–coupled showerhead (CCS) gas injection system enables the intermixing of precursors within close proximity to the substrates, resulting in uniform deposition. In addition, a three–zone heater design allows customized temperature profile across a wafer to further control uniformity of epitaxial layers. In this thesis, a Thomas Swan (now AIXTRON) 6 × 2" rotating disk CCS reactor is used. A Laytec in–situ optical monitoring system, with EpiTT and EpiCurve systems, provides real–time data collection for substrate temperature, wafer curvature, and reflectivity probing at wavelengths of 633 nm and 950 nm. These parameters allow us to extract the growth rate of the film and to monitor the growth chamber conditions.

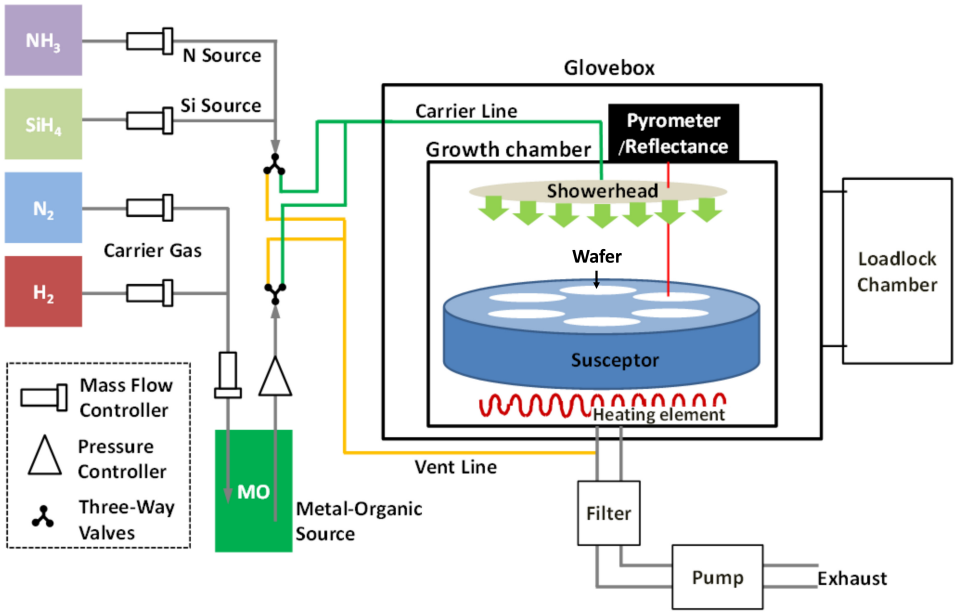

Figure 3: A simplified schematic diagram of an MOCVD reactor.

CHAPTER II

MATERIAL CHARACTERIZATION

Once the material is grown, it is very important to study the material quality, electrical, and optical characteristics then correlate the results to growth conditions for optimization. In this chapter, the basic methodologies used to characterize the epitaxial material is presented, including atomic–force microscopy (AFM), electroluminescence (EL), Hall–effect measurement, photoluminescence (PL), secondary ion mass spectrometry (SIMS), transmission electron microscopy (TEM), transmission–line measurement (TLM), and X–ray diffraction (XRD).

2.1 Atomic Force Microscopy

AFM or scanning force microscopy (SFM) provides three-dimensional mapping for a specimen surface with sub–nanometer resolution scale. The precursor of the AFM, scanning tunneling microscope, was invented in 1981 by Gerd Binnig and Heinrich Rohrer [23] who earned Nobel Prize in Physics in 1986. Later, Binnig, Quate, and Gerber invented the first AFM in 1986 [24], which consisted of five major components: a cantilever, probe tip, sample stage, measurement device, and feedback mechanism as shown in Fig.4.

The most important component of the microscope system is the cantilever with the probe tip at its end, which is used to scan a specimen surface. The cantilever is typically made of silicon or silicon nitride (Si_3N_4) and some of cantilevers have aluminum or gold as reflex coating, which is used to enhance the reflectivity of the back side of cantilevers as well as the signal deflected to detector. Because AFM relies on the forces between the probe tip and the specimen, knowing these forces, including mechanical contact force, van der Waals force, capillary force, chemical bonding force,

electrostatic force, magnetic force, Casimir force, and solvation force, is important for proper imaging. Thus, the cantilever is designed to detect forces in the range of 10^{-8} to 10^{-12}N while the deflections are limited to as small as $10^{-4}\mathring{A}$. Probe tip is usually in pyramid shape with 3 to 6 μm height and 15 to 40 nm end radius. Ideally, the probe tip should only have "ONE" atom at its apex for maximum resolution.

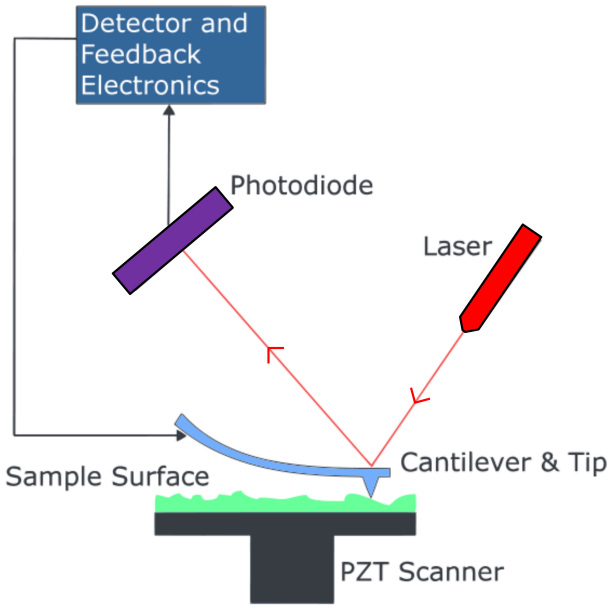

Figure 4: Schematic diagram of an AFM system using laser beam deflection detection.

In this thesis, a Veeco Dimension 3100 scanning probe microscope is used. It supports two main operation modes, i.e., contact mode and tapping mode. Figure 5 summarized the distance and the interatomic force, also known as Lennard–Jones potential curve, for the main operation modes. Contact mode is the first and foremost mode of operation and it is also the most common mode of operation. During the operation, the tip is kept in physically contact with specimen surface and a piezoelectric crystal is used to control the distance between the sample and the tip for maintaining constantly contact. Due to the fact that the tip is in hard contact with the specimen surface, the stiffness of the cantilever needs to be less than the effective

spring constant holding atoms together, which is typically on the order of 1 – 10 N/m; thus, most contact–mode cantilevers have a spring constant < 1 N/m. Images are formed by mapping the cantilever deflection with respect to the position of the sample to its topography.

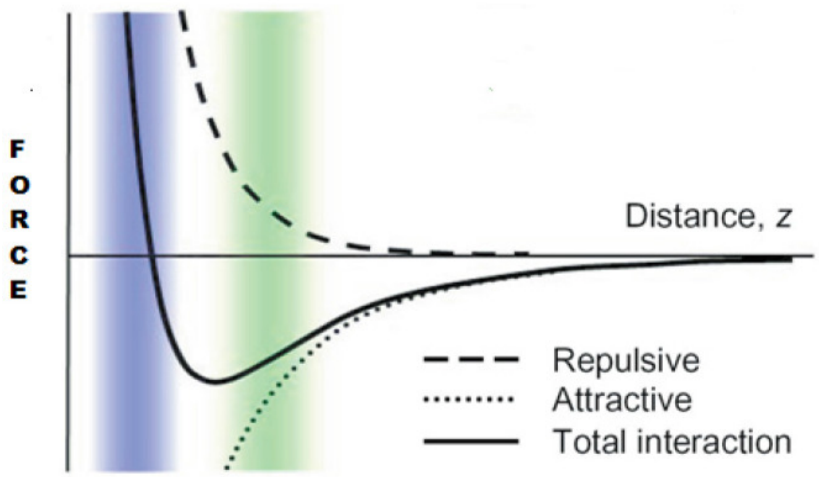

Figure 5: A tip–to–sample distance versus an interatomic force. For a tip–to–sample distance in blue region, microscope is operating under contact mode while in green region refers to non–contact mode. For intermittent–contact operation (tapping mode), tip–to–sample distance lies between contact mode and non–contact mode (white region between blue and green).

In the tapping mode operation, the cantilever is oscillating at its resonant frequency (typically from 100 to 500 kHz) which results in the probe tip "tapping" the surface with constant frequency. The feedback system will maintain the oscillation amplitude constant (typically 100 to 200 nm). Because the probe tip is not constantly physically in contact with sample, this technique allows high resolution topographic imaging of sample surfaces that are easily damaged. In addition, the high frequency makes the surface stiff (viscoelastic), and the tip-sample adhesion forces is greatly reduced; thus, tapping–mode inherently prevents the tip from sticking to the surface and causing damage during scanning. As a result, all the AFM images present in this

thesis are captured under tapping mode operation.

2.2 Electroluminescence

Electroluminescence (EL) is a widely used characterization methodology to analyze the electrical and optical properties of p–n junction devices. EL injects current into material through the electrical contacts, which are deposited on the contact layers by a CHA Solution electron beam (E–beam) evaporator and then thermally annealed by AnnealSys AS–One rapid thermal annealing (RTA) system. The carriers that are injected through the contacts will travel within the material and radiatively recombine to generate photons with an energy approximately equal to the material bandgap.

In this thesis, a Keithley 2400 DC power supply and an AVTECH pulsed current source are used as the sources for CW and pulsing measurement, respectively. Optical emission from the device is first coupled into a 600 μm diameter multimode optical fiber then passes through a SPEX 500M monochromator with a spectral resolution of 0.02 nm. The optical intensity at each wavelength is then analyzed by Hamamatsu R928 photomultiplier tube (PMT) and an Ortec 776 counter. For the optical polarization measurement, an α–BBO Glen–Laser polarizer with 100,000 : 1 extinction ratio is used to determined the optical polarization (transverse electric or transverse magnetic mode).

2.3 Hall–Effect Measurement

Hall–effect measurement is a method to measure the resistivity, majority carrier type, majority carrier concentration, and low–field carrier mobility of a given semiconductor. The most commonly used resistivity measurement technique is known as the van der Pauw method, which was first introduced by Leo J. van der Pauw in 1958 [25, 26]. Figure 6 shows the examples of possible sample configurations of van der

Pauw method. In this thesis, an approximately 1 × 1 cm^2 square sample is prepared. In the case of n–type AlGaN material, vanadium–based metal alloy is deposited (V/Al/Ti/Au for $300\mathring{A}/500\mathring{A}/300\mathring{A}/500\mathring{A}$) and then a two–step thermal annealling in a N_2 ambient is performed. The first annealing step is done at 450°C for 10 minutes and then the temperature is ramped to a higher temperature for another minute or less of anneal depending on the aluminum molar fraction.

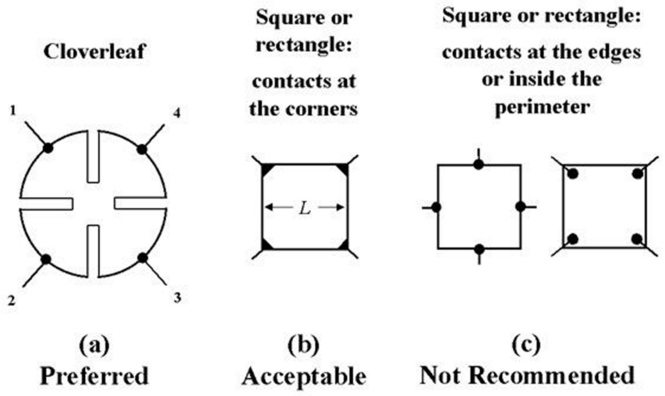

Figure 6: Examples of possible van der Pauw configurations and their preference.

For the p–type AlGaN, an extra step is required to prepare the Hall samples. Magnesium is the most commonly used acceptor in III–nitride material; however, it is compensated by hydrogen within the film during epitaxial growth [27]. In order to activate the acceptors, the hydrogen bond must be broken by methods such as low energy electron beam irradiation (LEEBI) [28] or thermal annealing [29]. In this work, wafers are first annealed in air for 3 minutes at 900°C before metal evaporation. The metal stack for p–type material uses nickel–based material (Ni/Ag/Pt for $50\mathring{A}/500\mathring{A}/200\mathring{A}$) and the annealing is done at ∼500°C in compressed air.

The experimental arrangement for resistivity measurements using van der Pauw's method is shown in Fig.7. The current is first applied across contact 1 & 2 (I_{12}) and the voltage is measured across contact 4 & 3 (V_{43}). Next, the current is applied I_{14}

and voltage V_{23} is measured. The sheet resistivity (ρ_s) or bulk resistivity (ρ) can be calculated as

$$\rho_s = \rho/t = \frac{\pi}{2ln(2)}\left[\frac{V_{43}}{I_{12}} + \frac{V_{23}}{I_{14}}\right] F(Q) \quad (\Omega/\square) \tag{13}$$

where t is the thickness of the layer, Q and F coefficients corresponds to symmetry and correction factors, respectively.

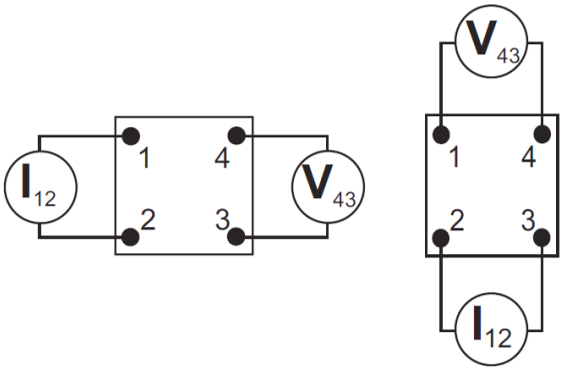

Figure 7: Schematic diagram of resistivity measurement using van der Pauw's method.

Correction factor (F) is used to described the geometrical asymmetry and not for material anisotropy or inhomogeneity. The symmetry factor Q is defined as (in the case shown in Fig.7)

$$Q = \frac{V_{43}I_{14}}{I_{12}V_{23}} \tag{14}$$

or its reciprocal, whichever is greater than 1. Assuming asymmetry coefficient is not too large (Q $<$ 10), F can be approximated as

$$F = 1 - 0.34657A - 0.09236A^2 \tag{15}$$

where A is

$$A = \left[\frac{Q-1}{Q+1}\right]^2 \tag{16}$$

When the current is fixed to a constant value for all six possible permutations, averaging the voltages V_{xy} measured for both current directions can be used to cancel thermoelectric and other effects; thus, Eq.13 and 14 can be reduced to

$$\rho_s = \frac{\pi}{2ln(2)} \left[\frac{(V_{43} + V_{23})}{I} \right] F(Q) \quad (\Omega/\square) \tag{17}$$

$$Q = \frac{V_{43}}{V_{23}} \tag{18}$$

The experimental setup for Hall effect measurement is shown in Fig.8. A constant current is injected at two non–adjacent contacts and the Hall voltage (V_h) is measured across the remaining contacts while a constant magnetic field B is applied perpendicular to the sample surface. The relation between magnetic and electrostatic forces can be related through the Lorentz Force equation given by

$$\overrightarrow{F} = q(\overrightarrow{E} + \overrightarrow{v} \times \overrightarrow{B}) \tag{19}$$

where q is the elementary charge, $\overrightarrow{E}$ is the electric field, $\overrightarrow{v}$ is particle velocity, and $\overrightarrow{B}$ is magnetic field. By setting the net force equal to zero, the electric field can be related to the magnetic field and the carrier velocity. The current can be calculated based on

$$\overrightarrow{I} = qNtW\overrightarrow{v} \tag{20}$$

where N is the carrier density, t is the thickness of the layer, and W is the separation between two contacts. Thus, the Hall coefficient (R_H) can be obtained by

$$R_{Hs} = R_H/t = \frac{1}{qN} = \frac{V_h}{IB} \quad (m^3/C) \tag{21}$$

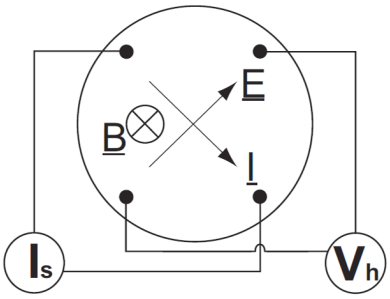

Figure 8: Generalized Hall effect measurement setup.

Once the Hall coefficient is obtained, the sheet carrier density (N_s) is related to Hall coefficient as

$$N_s = \frac{1}{qR_{Hs}} \tag{22}$$

Finally, the carrier mobility is calculated using

$$\mu = \frac{R_{Hs}}{\rho_s} \tag{23}$$

The Hall measurements carried out in this study were performed using an Accent HL5500PC Hall measurement system.

2.4 Photoluminescence

Photoluminescence (PL) is an optical characterization technique for estimating bandgap energy and defect levels in a semiconductor. In order to have radiative transitions, the optical excitation energy added to the semiconductor needs to be larger than the bandgap to promote an electron from valence band to conduction band, creating an electron–hole pair. For direct–bandgap semiconductors, most of the electron–hole pairs will recombine near the band edge, which will create photons with exactly same energy as the bandgap. The corresponding wavelength for a given photon energy (E) has a relation

$$E = h\nu = \frac{hc}{\lambda} \tag{24}$$

where h is Planck constant, ν is frequency of light, c is speed of light, and λ is the wavelength of light.

A Coherent COMPexPro 110 excimer laser is used as an excitation source in this study. The active gas used in this laser is argon fluoride (ArF), which emits at a wavelength of 193 nm ($h\nu \sim 6.4$ eV) under following reaction

$$2ArF \rightarrow 2Ar + F_2 + h\nu \tag{25}$$

The dimensions of the incident laser beam is 24 (mm) $\times$ 10 (mm) with pulse duration of 20 ns. The laser output power can range from 20 mJ to 200 mJ while the repetition rate can be set from 1 Hz to 100 Hz. The optical emission from the semiconductor sample is collected into a 600 μm diameter multimode optical fiber then analyzed with an Ocean Optics Maya 2000 Pro UV spectrometer with spectral range from 200 nm to 400 nm and $\sim$ 0.1 nm resolution. For the optical polarization characterization, an α–BBO Glen–Laser polarizer with 100,000 : 1 extinction ratio is used.

2.5 Secondary Ion Mass Spectrometry

Secondary Ion Mass Spectrometry (SIMS) profiling is a method used to measure the specific atomic concentration in a sample as function of depth. The background impurity concentrations, materials compositions, layer thickness, and doping concentrations in the epitaxial layers can be measured simultaneously; however, this is a destructive process.

Typically, a SIMS system consists of a primary ion gun, primary ion column, high vacuum chamber and secondary ion extraction lens, mass analyzer, and ion detection unit. The primary ion gun generate a primary ion beam composed of species such as O_2^+ or Cs^+ to sputter the sample layer by layer. Oxygen primary ions are often used to investigate electropositive elements due to an increase of the generation probability of positive secondary ions, while caesium ions are commonly

used to detect electronegative elements. All the atoms and molecules released from the sample surface are known as secondary ions.

For a given SIMS system, there are three basic analyzers available: sector, quadrupole, and time-of-flight (TOF). In this thesis TOF mass spectrometry is used, all ions are accelerated by an electric field with known strength and the acceleration results in an ion having the same kinetic energy as any other ion that has same charge. The time that it subsequently takes for the particle to reach a detector at a known distance is measured and this time is related to the mass–to–charge ratio of the particle (heavier particles have lower speeds), which allow us to identify ions.

As the sample is sputtered, the ion counts are plotted as a function of time for the ions of interests. At the end of sputtering, the depth of sputtering is calibrated by profilometer to convert from time profile to depth profile. In addition, the concentration of each ions are converted to elemental concentration (ions/cc) under following equation:

$$C_E = RSF\frac{I_E C_M}{I_M} \tag{26}$$

where C_E is the concentration of the element of interest, RSF is the abbreviation of relative sensitivity factor, I_E is the secondary ion intensity, C_M is the major/matrix element concentration, and I_M is the ion intensity of major element. IONTOF Time–of–Flight SIMS is used to collect some of data for relatively comparison in this work.

2.6 Transmission Electron Microscopy

The resolution of an optical system is limited by the Rayleigh criterion:

$$\delta = \frac{0.61\lambda}{n\sin\theta} \tag{27}$$

where λ denotes the wavelength of the optical system, n is index of refraction of the optical lens, and θ refers to the half-angle of the maximum cone of light that can enter or exit the lens. The Rayleigh criterion limits the optimal resolution for an

optical ultraviolet microscope to be $\sim$ 200 nm. In order to achieve atomic resolution, an even shorter–wavelength microscopy system is required. Utilizing de Broglie's equation for the wavelength of electrons, Max Knoll and Ernst Ruska in 1931 built the first transmission electron microscope (TEM) [30]. The electron wavelength is related to the electron's kinetic energy by the following relationship

$$\lambda = \frac{h}{\sqrt{2m_e q U_0 (1 + \frac{qU_0}{2m_e c^2})}} \tag{28}$$

where h is Plank's constant, m_e is the electron mass, q is the unit charge, U_0 is the accelerated voltage, and c is the speed of light. Equation 28 suggests that sub–angstrom electron wavelengths can be easily achieved under sufficient bias; therefore, a sub–angstrom resolution microscopy system can be realized.

To achieve high resolution, a TEM system utilizes an electron beam for imaging; therefore, it is crucial to understand the interaction between the electrons and the sample. Figure 9 shows a schematic diagram of the generated signals from a thin specimen under a high–energy beam illumination. The backscattered electrons (BSE) and secondary electrons (SE) can be detected with a scanning electron microscope (SEM). Energy–dispersive X–ray spectroscopy (EDS, EDX, or XEDS) detects the characteristic X–rays for elemental analysis or chemical characterization. The transmitted direct beam is the most important signal for TEM imaging since it carries atomic level information of the sample. Inelastically scattered electrons are important for another type of TEM imaging known as scanning transmission electron microscope (STEM). STEM measurements allow some important materials analysis techniques, including energy dispersive X–ray (EDX) spectroscopy, electron energy loss spectroscopy (EELS), and annular dark-field imaging (ADF).

In the TEM system, electrons can be generated by two different methods, thermal emission and field emission. Typically, thermal emission sources have shorter lifetime and operating at higher temperature; however, the guality of the vacuum

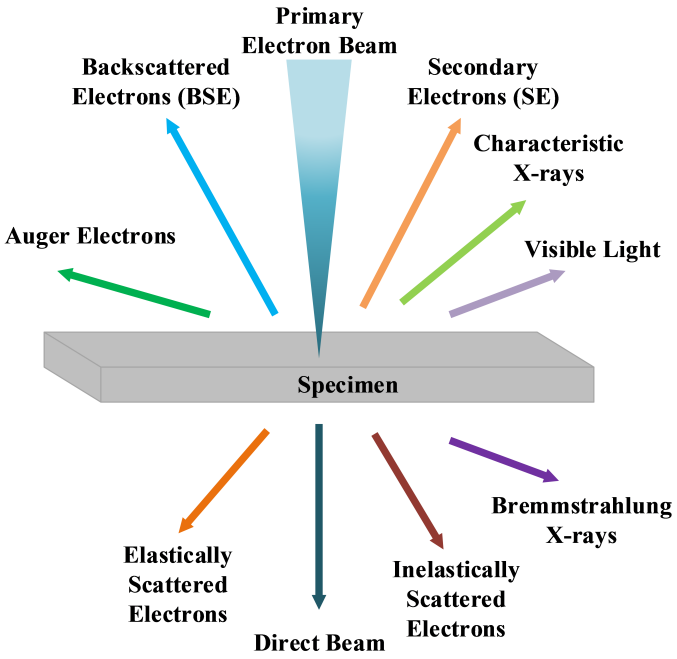

Figure 9: Signals generated when a high–energy electron beam interacts with a thin specimen. Most of these signals can be detected in different types of electron microscopy systems.

environment is not as critical as for field emission sources. Since electrons are used as the electromagnetic source for a TEM system, the optical lens in the conventional microscope needs to be replaced by an electrons lens. However, the refraction of the electron beam passing through different mediums is still governed by the Snell's law. Figure 10 shows the schematic outline of a TEM system.

A typical TEM system has three main apertures, the condenser aperture (CA), the objective aperture (OA), and the select–area (SA) aperture. The SA aperture is used to acquire select area diffraction patters (SADP), which is extremely important to determine the zone axis and crystal structure. The OA is located at the back focal plane of objective lens and it is used to determine the imaging modes of microscope, bright field, dark field or diffraction mode. Lastly, CA is employed to control the brightness of the image. The operating mode that offers the best resolution images

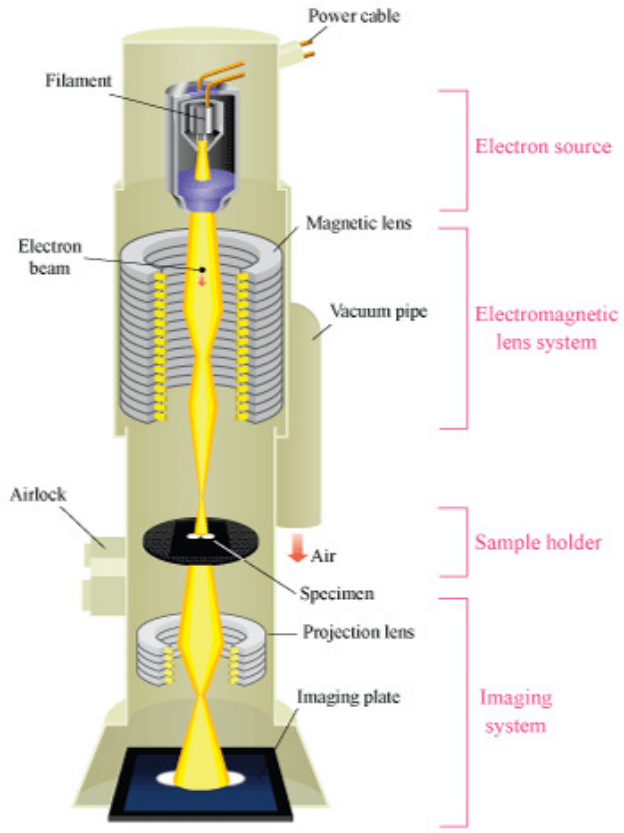

Figure 10: The schematic diagram of a TEM.

in a given microscope is known as high–resolution transmission electron microscopy (HRTEM), which measures the phase contrast from the transmitted beam of "thin" specimen. On the other hand, STEM rasters the beam across the sample and a very powerful characterization technique that uses a STEM system is high-angle annular dark-field imaging (HAADF). The image from HAADF is directly related to the atomic number (Z); therefore, relative composition between layers from same type of alloy can be easily determined.

The TEM images and analysis presented in this work was performed by our colleagues at Arizona State University under Professor Fernando A. Ponce.

2.7 Transmission–Line Measurement

Transmission–line measurement (TLM) is developed for measuring the sheet resistance of the semiconductor (R_{sh}) and the the specific metal–semiconductor contact resistance (ρ_c). The metal patterns are created via ultraviolet photolithography process. First, 2 layers of photoresist, LOR5B and S1813, are coated on the wafer using a CEE 100 spin coater. The TLM patterns are structured using a Karl Süss MJB–3 mask aligner for UV–lamp exposure. In order to remove the unwanted photoresist, the wafer needs to go through development and descum processes to insure the patterns are sharp. Standard metal evaporation and rapid thermal annealing (RTA) are performed as described in section 2.3 Hall measurement; however, an extra step is performed before metal annealing, which is called lift–off. Lift–off process is to remove all the photoresist and the areas of unwanted metal stacks. The following discussion separates TLM patterns into two categories based on the shape of metal contact.

2.7.1 Rectangular Transmission–Line Measurement

The first type of pattern consists of rectangular metal pads as shown in Fig.11. A mesa etching of the semiconductor around the pattern is required to avoid the possibilities of fringe effects, which alters the measurement results. After obtaining the resistance

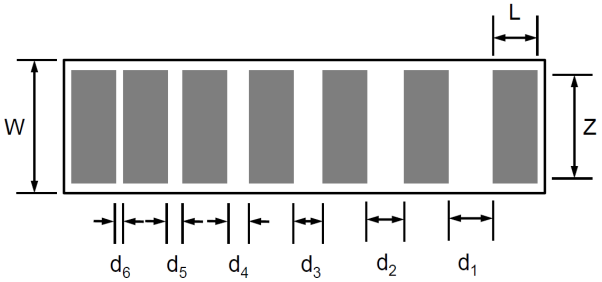

Figure 11: A typical rectangular TLM pattern showing the differences in metal contact pads spacings.

for all different metal pads spacings, the specific contact resistance (ρ_c) and the sheet resistance (R_{sh}) can be obtained by plotting the resistances as a function of metal–pads spacing as shown in Fig.12. The sheet resistance of semiconductor material can

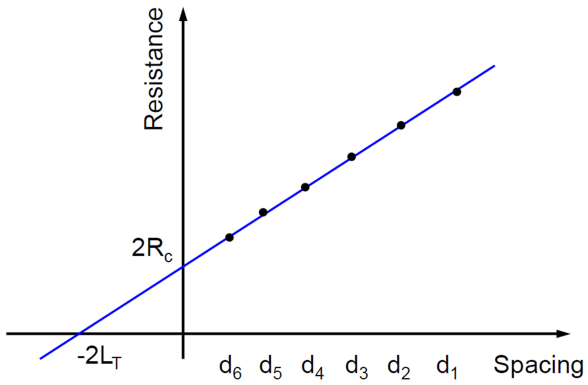

Figure 12: An example plot of measured resistances as function of spacing.

be obtained from the following equation:

$$R_{sh} = slope \times Z \quad (\Omega/\square) \tag{29}$$

where Z is the length of the metal pads as shown in Fig.11. When the contact separation becomes zero, the intercept of the line at the y–axis (resistance axis) corresponds to twice the contact resistance, $2R_c$. On the other hand, when the resistance becomes zero, the intercept of the line at the x–axis (metal–pads spacings) is two times the transfer length, $2L_T$. The specific contact resistance can be calculated as:

$$\rho_c = R_c \times Z \times L_T \quad (\Omega - cm^2) \tag{30}$$

The rectangular TLM pattern used in this thesis has metal pad dimensions $L = 50\mu m$ and $Z = 80\mu m$ while the spacings are 4 μm, $8\mu m$, 16 μm, and 32 μm.

2.7.2 Circular Transmission–Line Measurement

Unlike rectangular TLM pattern, circular TLM (CTLM) doesn't require a mesa etching since the pattern itself eliminates the possibilities of fringe effect [31]; however, CTLM usually has larger patterns, which require more wafer area compared to linear (rectangular) TLM. A CTLM test structure consists of a metal stack for circular inner region with radius L, a gap of width d, and a metal stack for outer region as shown in Fig.13. The total resistance between the internal and the external contact can be

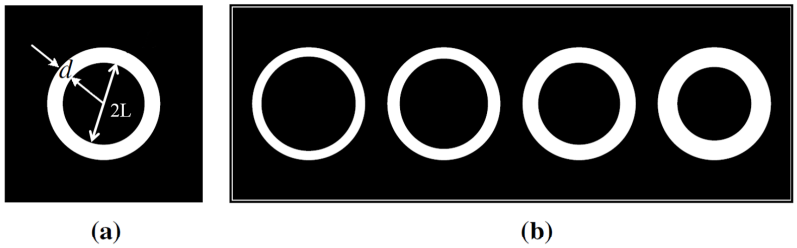

Figure 13: An example of CTLM test structure. The dark regions represent metal contacts. Spacing d and radius of inner circle are shown in panel (a).

formulated as:

$$R_T = \frac{R_{sh}}{2\pi}\left[\frac{L_T}{L}\frac{I_0(L/L_T)}{I_1(L/L_T)} + \frac{L_T}{L+d}\frac{K_0(L/L_T)}{K_1(L/L_T)} + ln\left(1+\frac{d}{L}\right)\right] \tag{31}$$

where L_T is known as transfer length, I and K denote the modified Bessel functions of the first order. In the practical design L $\ll$ 4L$_T$, the Bessel function ratios I_0/I_1 and K_0/K_1 tend to become unity, which simplifies Eq.31 to:

$$R_T = \frac{R_{sh}}{2\pi}\left[\frac{L_T}{L}\frac{L_T}{L+d} + ln\left(1+\frac{d}{L}\right)\right] \tag{32}$$

The only two unknowns in the Eq.32, R_{sh} and L_T, can be calculated based on the total resistance measurement on different spacings. The specific contact resistance holds a relation:

$$\rho_c = L_T^2 R_{sh} \tag{33}$$

The CTLM test structure performed in this work has $L+d = 120\mu m$ or $L+d = 200\mu m$ while the spacing d varies from 4 μm, 8μm, 16 μm, 32 μm, and 64 μm.

2.8 X–Ray Diffraction

X–ray diffraction (XRD) is a non–destructive process used to analyze the thickness, lattice parameters, strain, composition, degree of relaxation, and defect densities of epitaxial layers and device structures. In this work, all the XRD scans were measured by a Phillips X'Pert MRD (Material Research Diffractometer) High Resolution X–ray diffractometer (HRXRD). The X–ray source is generated from Cu $K_{\alpha 1}$ transition, which emits X–ray with wavelength of 1.540562 $\mathring{A}$. The X–ray beam is then collimated by 4–bounce Ge(220) Bartels monochromator before impinging on the sample. Once the beam is "diffracted" from the sample, two different diffracted beam paths are available. The main difference is that one of the diffracted beam paths has an analyzer crystal (or known as beam conditioner) installed, which provides a beam with an angular resolution below 1 arcsec. A typical configuration of a HRXRD measurement system is shown in Fig.14.

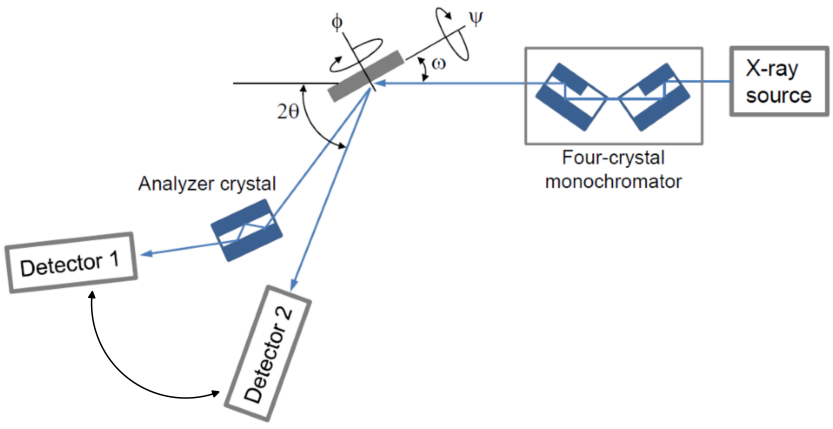

Figure 14: Schematic diagram for a typical HRXRD measurement system.

The fundamental process employed in XRD is probing a crystal with X–ray radiation having a wavelength (λ) smaller to the crystal lattice spacing, as shown in Fig.15. When the X–rays are scattered by the electron cloud surrounding each atom in the crystal, constructive interference occurs if and only if the the path length difference is equal to $2d\sin\theta$, which is also known as Bragg's law. Experimentally, the angle 2θ is measured and the diffraction pattern is related to the spacings of the crystal planes and size of crystallites. In order to investigate different diffraction spots, measurement angles (ω, 2θ, ϕ, and ψ) are altered to meet the Bragg condition, as shown in Fig.14.

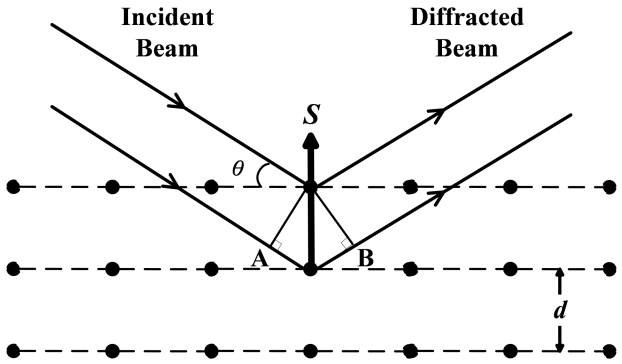

Figure 15: The Bragg condition for diffraction is shown. AB is defined as the path length difference (nλ), d is crystal plane spacing, θ defines the angle between incident beam and the crystal plane, and $\vec{S}$ represents scattering vector.

By sweeping different angle or angles for diffraction, the XRD measurement provides various information about the material. For instance, ω-scans are usually used for measuring the film quality since the diffraction peak broadening by dislocations can be easily seen. On the other hand, ω–2θ or 2θ–ω scans probe the diffraction spots along the direction that typically has less broadening; thus, these scans are usually used for lattice parameter or composition determination. Both ω and ω–2θ scans are also known as "rocking curves", as both scans involve 'rocking' the sample about the ω–axis. Table 3 summarized different scan types that are commonly used in XRD

[32].

Table 3: Summary of different scan types available on high–resolution X–ray diffractometers [32].

Scan type	Description
2θ–ω	The sample is rotated by ω and the detector is rotated by 2θ with an angular ratio of 1 : 2. In reciprocal space, scattering vector ($\vec{S}$) moves outwards from the origin. The length of $\vec{S}$ changes, but its direction remains the same and depends on the offset. For 2θ–ω scans, the x–axis is in units of 2θ, whereas for ω–2θ, the x–axis is in units of ω. When there is no offset and $\omega = \theta$ this is a symmetrical scan (θ–2θ) which is vertical in reciprocal space. Standard scan type for powder diffraction.
ω–2θ	Simply a 2θ–ω scan, but with ω on the x–axis. Standard scan type for reflectivity and high–resolution work.
2θ	The sample and source remain stationary and the detector is moved. $\vec{S}$ traces an arc along the circumference of the Ewald sphere. Both the length and the direction of $\vec{S}$ change.
ω	The detector remains stationary and the sample is rotated about the ω axis. In reciprocal space, $\vec{S}$ traces an arc centered on the origin. The length of $\vec{S}$ stays the same, but its direction changes.
Q	Software can be used to scan ω and 2θ in non–integer ratios, scanning $\vec{S}$ along a given direction in reciprocal space. Reciprocal space maps of any desired shape can then be collected.
ϕ	Rotation of the sample about the ϕ axis. The length of $\vec{S}$ stays the same, but the sample is moved, bringing the reciprocal lattice spot through $\vec{S}$ so that the direction of $\vec{S}$ changes with respect to the sample.
χ	Similar to ϕ scans, except that the sample is rotated about the χ axis.

In order to understand the information on interplanar spacings and defect–related broadening, a reciprocal space map (RSM) can be used to verify the information. An RSM consists of a series of ω–2θ scans at successive ω values and presents the results in map form. An RSM measurement is recorded in angular units; thus, the units should be converted into reciprocal lattice units (RLUs) for proper analysis. The following equations relate the coordinates of the reciprocal point (Q_x, Q_y) with

the angular units ω and 2θ:

$$Q_x = \frac{2\pi}{\lambda}\left[\cos\omega - \cos(2\theta - \omega)\right] \tag{34a}$$

$$Q_y = \frac{2\pi}{\lambda}\left[\sin\omega + \sin(2\theta - \omega)\right] \tag{34b}$$

Figure 16 shows an example of RSM for AlGaN grown on AlN template on sapphire substrate. The Q_y axis represents the reciprocal lattice constants in the vertical direction (c–axis), which indicates the difference in the composition. On the other hand, difference in Q_x axis refers to the difference in the in–plane lattice constant (a–axis), which is a very important parameter to determine the in–plane percentage relaxation ($R_{\%}$). The percentage relaxation can be calculated as [33]

$$R_{\%} = \frac{d_{\parallel}^{L(meas)} - d_{\parallel}^{Sub(meas)}}{d_{\parallel}^{L(0)} - d_{\parallel}^{S(0)}} \times 100 \tag{35}$$

where $d_{\parallel}$ is the in–plane lattice spacing and superscripts L denotes layer, Sub denotes substrate, 0 refers to to reference lattice parameter, and $meas$ represents the measured value.

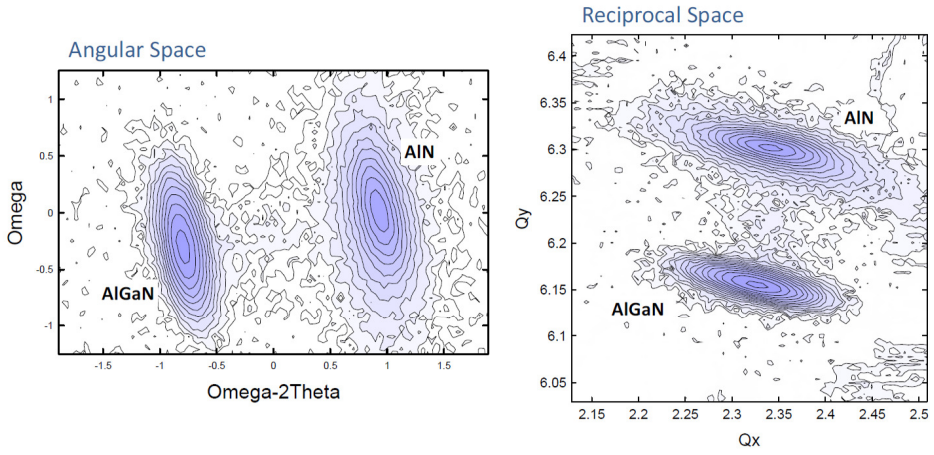

Figure 16: The angular and reciprocal space representation of an RSM measurement.

In order to calculate the percent relaxation of the layer, a method to determine the lattice parameter is required. From Bragg's law ($n\lambda = 2d_{hkl}\sin\theta$), the angle

θ is required for obtaining the distance d_{hkl} between a particular set of planes. In the hexagonal material system, the following equation relates the d_{hkl} to the lattice parameters a and c

$$\frac{1}{d_{hkl}^2} = \frac{4}{3}\frac{h^2 + k^2 + hk}{a^2} + \frac{l^2}{c^2} \tag{36}$$

Since there are two lattice parameters (unknowns) to be determined, two d_{hkl} measurements are required. Typically, one high–angle "symmetric" reflection is measured (e.g., d_{0002}), from which the lattice constant c can be found directly. Then another high–angle "asymmetric" reflection is measured (e.g., $d_{20\bar{2}4}$). Using the value of c found previously, the lattice constant a can be extracted. Utilizing Eq.35, the composition and the relaxation of the film grown on the substrate can be obtained.

As mentioned earlier, the XRD measurements performed in this work are taken using a Philips X'Pert MRD HR–XRD with a Cu $K_{\alpha 1}$ source and four Ge (220) crystals as the beam monochrometer. The system is equipped with two separate detector optics; beam path 2 has a typical configuration used for the rocking curve scans, while beam path 1 is equipped with a Ge (110) channel–cut crystal that is aligned to the (220) reflection as an analyzer crystal for the RSM scan.

CHAPTER III

OPTICAL EMITTER DEVICE PHYSICS

This chapter will review the basic device physics for semiconductor optical emitters, including light emitting diodes and laser diodes.

3.1 Light Emitting Diode

3.1.1 Radiative Transitions

A light emitting diode (LED) is a p–n junction device that converts electrical energy into optical radiation. Figure 17 schematically demonstrates the basic recombination transitions of excess carriers in a semiconductor. These transitions may be classified as follows. The first classification (1) is the interband transition: (a) intrinsic emission corresponding very closely in energy to the bandgap, and (b) higher–energy emission involving energetic carriers. The second class (2) is the transitions involving chemical impurities or physical defects, including (a) conduction band to acceptor–type defect, (b) donor–type defect to valence band, (c) donor–type to acceptor–type defects, and (d) band–to–band via deep–level traps. The last classification (3) is the intraband transition involving Auger recombination process. In order to emit photons efficiently, material is required to have radiative transitions predominate over nonradiative ones and the most preferable radiative process is (a) in classification (1).

There are three main optical processes for interactions between a photon and an electron in the material as shown in Fig.18: (a) A photon is absorbed by the excitation of an electron from the valence band to the conduction band. (b) An electron in the conduction band can spontaneously return to an empty valence band state (recombination) and the energy differences between the conduction band to the valence band is released as a photon. (c) The incoming photon stimulates the electron

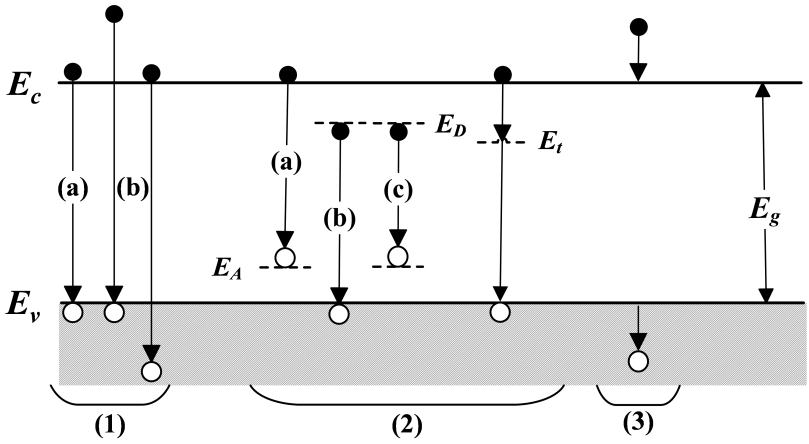

Figure 17: Basic recombination transitions in semiconductor. E_D, E_A, E_t are donor–type, acceptor–type, and deep–level traps respectively.

in the conduction band return to the valence band by producing another photon with same photon energy, phase, polarization, and the direction of the incoming photon. In this section, the discussion will be focusing on process (b) since it is the main process in a LED.

3.1.2 Device Structures

The basic structure of a LED is typically a composed of a p–n homojunction or a p–i–n heterojunction structure. Under forward bias, minority carriers are injected from both sides of junction. At the vicinity of the junction, there is an excess of carriers, and recombination will take place. In the case of p–i–n junction, an undoped thin layer is bound by layers with a higher energy gap forming type–I heterojunctions, which allows better efficiency for recombination processes. If the "thin" undoped layer has a thickness in the range of 10 nm or smaller, a quantum well is formed. The quantum–well design allows for better carrier confinement, resulting higher probabilities for radiative recombination processes. In addition, the quantum–well design reduces the amount of active material, which leads to better performance and efficiency for optical emitters.

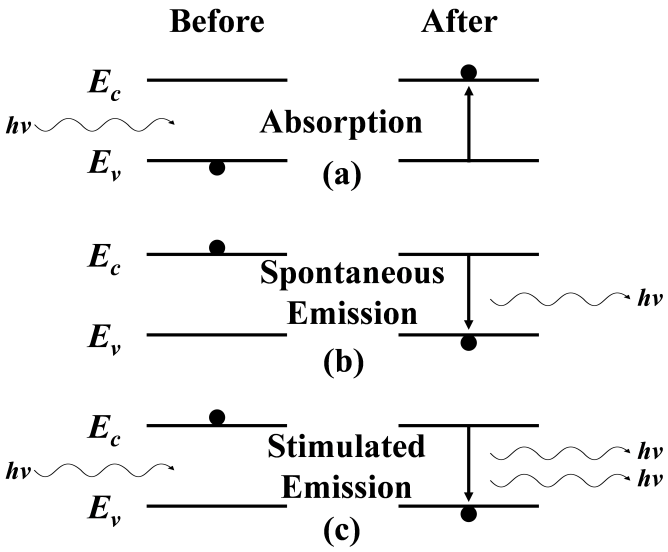

Figure 18: The three basic optical process between two energy levels. The black dot denotes the energy state of the electron.

To characterize device performance for further optimization, different terms relating to LED efficiencies are discussed.

3.1.2.1 Internal Quantum Efficiency

The internal quantum efficiency (η_{in}) characterizes the efficiency of converting excess carriers to photons, defined as

$$\eta_{in} = \frac{\text{number of photons emitted internally}}{\text{number of carriers passing junction}} \tag{37}$$

Since the carriers at the junction can undergo either radiative or non–radiative recombination processes, η_{in} can be related in terms of recombination process lifetimes as

$$\eta_{in} = \frac{R_r}{R_r + R_{nr}} = \frac{\tau_{nr}}{\tau_{nr} + \tau_r} \tag{38}$$

where R_r and R_{nr} are the radiative and non–radiative recombination rates, and τ_r and τ_{nr} are their associated radiative and non–radiative lifetimes, respectively. The radiative lifetime τ_r is inversely proportional to the recombination coefficient and the

non–radiative lifetime is inversely proportional to the product of trap density (N_t) and capture cross section (σ).

3.1.2.2 External Quantum Efficiency

For LED applications, an important consideration is the light emitted external to the device. The parameter that measures the efficiency of getting the light out externally is the called optical efficiency (η_{op}), which is also known as extraction efficiency. The net external quantum efficiency, η_{ex}, is defined as

$$\eta_{ex} = \frac{\text{number of photons emitted externally}}{\text{number of carriers passing junction}} = \eta_{in}\eta_{op} \tag{39}$$

3.1.2.3 Optical Efficiency

The optical efficiency is a subject of optics inside and around the devices, totally independent of electrical performance. Three major loss mechanisms limit the optical efficiency: (1) absorption loss within the LED material, (2) Fresnel loss, and (3) critical–angle loss. For Fresnel loss and critical–angle loss, the most important phenomena arises from Snell's law, which governs the refraction of light at the semiconductor and ambient interface. Applying the phase matching condition for the electromagnetic (EM) field at the interface, the reflection coefficient can be derived. Depending on the angle of the incidence, the direction of path may or may not change; however, in either cases, the EM wave suffers from the Fresnel loss due to the reflection at the boundary. In the more extreme case, when the incident angle is larger than "critical angle", all the light suffers a phenomena known as total internal reflection. The critical angle is function of semiconductor (n_s) and ambient (n_0) refractive indexes, which can be formulated as

$$\theta_c = \sin^{-1}(n_0/n_s) \tag{40}$$

3.1.2.4 Power Efficiency

The power efficiency (η_p), also known as wall–plug efficiency, is defined as the ratio of the light power output to the electrical power input,

$$\eta_p = \frac{\text{optical power out}}{\text{electrical power in}} = \frac{\text{output optical power}}{\text{number of carriers passing junction} \times q \times V} \tag{41}$$

3.2 Laser Diode

Semiconductor lasers are important optoelectronic devices for communication, sensing, optical data storage, etc. Similar to other lasers, optical radiation from a laser diode has spatial and temporal coherence, which produces a highly monochromatic and directional beam of light. As mentioned earlier, the dominant recombination mechanism in a LED is spontaneous emission. In the case of stimulated emission, a photon impinges on an electron while it is still in the conduction band. The electron in the conduction band is immediately stimulated to make its transition to the ground state and gives off another photon of the same wavelength and is in phase with the incident radiation. Notice there are two interesting properties of the stimulated emission. First, one photon input is needed and it becomes two photons in the output, which is a basic concept of optical gain. Second, the two photons are in phase, making the laser output coherent. In the following, important laser structure components and device characteristics will be discussed.

3.2.1 Optical Resonator

A structural requirement for a laser is an optical resonator in the direction of the light output. The optical resonator mainly serves to trap the light and build up the intensity within the cavity. The majority of semiconductor lasers form a Fabry–Perot etalon by fabricating two mirror–like smooth walls perpendicular to the junction. The reflectivity of these mirrors (facets) play a vital role in laser operation as it determines

the threshold modal gain (G_{th}) for lasing with following relationship

$$G_{th} = \alpha_i + \frac{1}{2L} ln \left(\frac{1}{R_1 R_2} \right) \tag{42}$$

where L is the cavity (resonator) length, α_i represents the intrinsic loss, and the two Rs are the reflectivity for the front and rear facets.

3.2.2 Waveguide

In the previous section, an optical resonator which traps the light within cavity in longitudinal direction was discussed. This section, the confinement of light in the direction parallel to the direction of light propagation will be discussed. Due to the non–uniform refractive indexes near the light–emitting junction, a waveguide can be formed for optical confinement. This is particularly important for double–heterojunction lasers as the active layer can be formed with material of higher refraction index than the surrounding layers, thereby forming a waveguide.

Since the optical field pattern is distributed throughout the device, a characteristic optical confinement factor (Γ) is defined to determine the fraction of optical intensity within the active region. Mathematically, Γ can be defined as

$$\Gamma = \frac{\int \int_{\text{active region}} |E(x,y)|^2 dxdy}{\int \int |E(x,y)|^2 dxdy} \tag{43}$$

Since the Poynting vector is proportional to $|E(x,y)|^2$, threshold gain (g_{th}) can be determined based on Eq.42

$$G_{th} = \Gamma g_{th} = \alpha_i + \alpha_m \tag{44}$$

$$\alpha_m = \frac{1}{2L} ln \left(\frac{1}{R_1 R_2} \right) \tag{45}$$

Notice that a larger optical confinement factor leads to a smaller threshold gain and this is due to the fact that the optical intensity within the resonator can build up faster with more photons confined in the active region. This observation also demonstrates the importance of the heterojunction as it can provide $\sim 10\%$ index contrast while the homojunction only offers 0.1% to 1% of index contrast.

3.2.3 Laser Characteristics

When the device is operating below threshold, the output light is mainly spontaneous emission. For a further increase in the injection current to the above threshold condition, the light output intensity P_{out} versus the injection current (L–I curve) is determined by

$$P_{out} = \eta_i \frac{\hbar\omega}{q} \frac{\alpha_m}{\alpha_m + \alpha_i}(I - I_{th}) \tag{46}$$

where η_i is internal quantum efficiency and $\frac{\hbar\omega}{q}$ represents the photon energy. The external quantum efficiency η_e is defined as

$$\eta_e = \eta_i \frac{\alpha_m}{\alpha_m + \alpha_i} \tag{47}$$

since the only extraction is due to mirror loss (α_m). Besides the extraction efficiency, the other efficiency parameter follow the discussion in the LED section.

3.2.4 Scaling Laws for Multi–Quantum Wells Lasers

In order to achieve a larger output power, a larger volume of active region is required. For a multi–quantum well (MQW) laser structure with n_w quantum wells and a cavity length L, the required modal gain G_{th} at threshold condition is

$$G_{th} = n_w \Gamma_w g_w = \alpha + \frac{1}{2L} ln\left(\frac{1}{R_1 R_2}\right) \tag{48}$$

where α is the internal optical loss, Γ_w is the optical confinement factor per well, g_w is "material " gain per well, and both Rs are the optical power reflection coefficients at the facets. Since the modal gain is scaled by the number of quantum wells, the threshold current density is also scaled by the number of quantum wells, which can be expressed as

$$\eta J_{th} = n_w J_w \tag{49}$$

where η is the injection quantum efficiency or the percentage of the injected carrier that gets captured by the quantum wells. Therefore, the material gain ($n_w g_w$) has a

relationship with the injection current density ($n_w J_w$) as

$$n_w g_w = n_w g_0 \left[ln \left(\frac{n_w J_w}{n_w J_0} \right) + 1 \right] \tag{50}$$

Notice g_0 and J_0 are device specific fitting parameters. The threshold current density can be obtained as

$$J_{th} = \left(\frac{n_w J_0}{\eta} \right) exp \left[\left(\frac{1}{n_w \Gamma_w g_0} \right) \left(\alpha + \frac{1}{2L} ln \frac{1}{R_1 R_2} \right) - 1 \right] \tag{51}$$

Taking logarithm function of J_{th},

$$ln J_{th} = ln \left(\frac{n_w J_0}{\eta} \right) + \frac{\alpha}{n_w \Gamma_w g_0} + \frac{L_{opt}}{L} - 1 \tag{52}$$

where L_{opt} is the optimum cavity length and it is defined as

$$L_{opt} = \frac{1}{2} \frac{1}{n_w \Gamma_w g_0} ln \left(\frac{1}{R_1 R_2} \right) \tag{53}$$

Substituting the optimal cavity length to the threshold current density equation, the minimum threshold current is then given as

$$I_{th}^{min} = \frac{1}{2} \left(\frac{w J_0}{\eta \Gamma_w g_0} \right) ln \left(\frac{1}{R_1 R_2} \right) exp \left[\frac{\alpha}{n_w \Gamma_w g_0} \right] \tag{54}$$

Assuming the loss coefficient (α) and other parameters such as Γ_w, J_0, η, and g_0 are independent of the number of wells. An optimal number of wells (n_{opt}) can be found such that I_{th} is minimized, ($\partial I_{th} / \partial n_w = 0$)

$$n_{opt} = \frac{1}{\Gamma_w g_0} \left(\alpha + \frac{1}{2L} ln \frac{1}{R_1 R_2} \right) \tag{55}$$

3.2.5 Technical Challenges

3.2.5.1 Strain–Induced Defects

As mentioned earlier, laser diodes have more structural requirements than LEDs; therefore, a more complex epitaxial structure and fabrication process are required. In addition, the heterostructure growth usually comes associated with lattice mismatch.

If the overall structural strain exceeds a critical limit, it can lead to crystal lattice relaxation, which usually is accompanied with dislocations and/or cracking. These dislocations serve as non–radiative recombination centers and can limit the efficiency of the optical processes in the device.

The commonly used substrate for III–nitride material is sapphire because of its low cost and availability. However, the in–plane lattice mismatch between sapphire and AlN is about 14%. This results a built–in strain in the epitaxial layers and increased formation of defects. In order to alleviate the defect and strain challenges, a native AlN substrate can be used instead. These native substrates can enable better device performance both optically and electrically due to a significant reduction in the strain and defects. However, these native substrates are still very rare, which significantly increases the cost for the device.

3.2.5.2 Quantum–Confined Stark Effect

The quantum–confined Stark effect (QCSE) describes the fact that in some cases, electron and hole wave functions in a quantum well are spatially split due to the presence of an applied electric field as shown in Fig.19. The transition rate for optical emission in the semiconductor is govern by Fermi's golden rule, which states that the transition rate is directly proportional to the spatial overlap between electron and hole wave functions. Thus, the band bending caused by QCSE results the red–shift in optical emission spectrum and more importantly, it drastically reduces the optical emission efficiency.

For the polar III–nitride materials, QCSE has larger impact on device performance compared to semiconductors with a zinc–blende structure or non–polar wurtzite structure and this is due the presence of a strong polarization field along the [0001] orientation. Even with no external bias is applied to the material, a strong polarization is generated through the spontaneous and piezo polarization [34, 35] which can be

as high as few MV/cm [36]. To obtain the optimal optical device performance, it is necessary to engineer the active region without polarization charge by polarization matching between well and barrier [37].

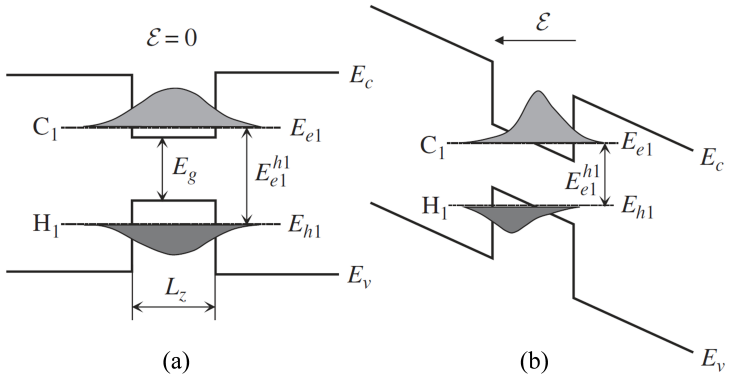

Figure 19: Quantum–well energy subbands and wave functions (a) in the presence of an applied electric field and (b) in the presence of an applied electric field.

CHAPTER IV

DEEP–ULTRAVIOLET EMITTERS

4.1 Growth on Native Substrates

One of technical challenges going toward shorter wavelength is lack of native substrates for III–nitride materials. A c–plane sapphire (Al_2O_3) is the most commonly used substrate due to its hexagonal structure, thermal stability, availability, and low cost. However, a significant lattice mismatch between AlN/GaN and the Al bonding sites on sapphire results in crystal strain and induces defect formations in the following epitaxially grown layers.

A major breakthrough occurred in 1985 as Amano and Akasaki demonstrated first high–quality GaN epitaxial films on sapphire using a low–temperature AlN buffer layer by MOCVD [38]. The purpose of low–temperature (LT) buffer layer allows the nucleation of 3D islands, which lowers the interfacial free energy between the substrate and the film. Later, the high–temperature layers grown laterally across the dense island cluster, which smooth the surface and results in a high-quality and uniform film. However, dislocation densities still remain high, which inhibits radiative transitions as these defect sites act as non–radiative recombination centers.

In order to avoid these defect centers, one solution is to use native AlN substrates. Advantages for growth on a native substrate enables homoepitaxial growth for the buffer layer [39], which significantly reduces the density of dislocations in epitaxial layers and the subsequent active region growth. In addition, reducing the differences in thermal expansion of materials eliminates formation of cracks during the thermal cycle and cool–down.

In this study, $\sim$ 550 μm thick of aluminum–polar (0001) AlN substrates were

used. Prior to growth, AlN substrates were etched in a 3:1 H_2SO_4: H_2PO_4 solution at 90°C for removing the native surface hydroxide [39]. The wafer is then annealed in a high–purity ammonia ambient at high temperature ($\sim$ 1100°C) for the optimal epitaxial–ready condition. The epitaxial growth was done in a Thomas Swan 6 $\times$ 2" close–coupled showerhead (CCS) metalorganic chemical vapour deposition (MOCVD) reactor. Due to the low ad–atom mobility of Al atoms on the growing surface, high growth temperature and low V/III ratio are required for two–dimensional growth and smooth surface formation [40]. In this work, the relatively high growth temperature of 1130°C was used while the V/III ratios for AlN buffer layer and AlGaN layers growth are set to less than 100 and approximately 400, respectively. The ideal temperature range for high aluminum mole fraction of AlGaN-based material could be above 1200°C; however, the limitations of this MOCVD reactor prevent us from performing such high temperature growth. SAFC Hitech® trimethylgallium (TMGa) and trimethylaluminum (TMAl) were used as alkyl group III precursors and ammonia (NH_3) as the group V hydride precursor. Silane (SiH_4) and bis–cyclopentadienyl magnesium (Cp_2Mg) were used for n–type and p–type doping, respectively.

Utilizing these growth parameters as basic template, various optically pumped and electrical injection DUV emitters were grown on AlN substrates. The first three structures are designed specifically as optically pumped DUV laser structures. Due to electron–hole pairs are generated based on absorption from external laser excitation, technical challenges for an electrical device become more manageable, including the required conductivity for waveguide layers, carrier distributions within quantum wells, and spill over current. The second part of this chapter will discuss the development for a diode emitter. To achieve highly conducting p–waveguide layer, an inverse tapered design was employed to transport holes efficiently to the active region [41]. Spill over current can be inhibited by graded–index separate–confinement heterostructure (GRINSCH) design for the active region. Lastly, the number of quantum well is

limited to four to ensure uniform carrier distribution within wells.

4.2 Sub–250 nm Optically–Pumped Laser

4.2.1 Sample 1-2643-1: 246.8 nm Optically Pumped DUV Laser

The epitaxial structure for the first optically pumped DUV laser of this study is illustrated in Fig.20. The active region consists of a ten-period multi–quantum well (MQW) structure, with 3 nm $Al_{0.60}Ga_{0.40}N$ wells and 5 nm $Al_{0.75}Ga_{0.25}N$ barriers, which emits photons near 250 nm. The active region is sandwiched between 200 nm AlN buffer layer and 10 nm AlN cap layer, which serve as surface passivation layer to prevent any possible oxidation of the active region. In addition, the cap layer also allows higher overlap between the optical field in the active region and the optical mode (known as optical confinement factor Γ); however, the thickness of cap layer is limited due to the absorption coefficient of the material at the external laser excitation wavelength of 193 nm. Since AlN has the smallest index of refraction at 250 nm, the omission of any buffer layer for strain management allows enhancement of the confinement factor.

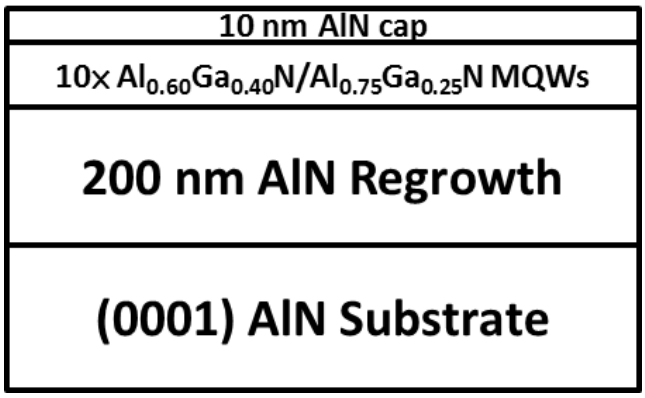

Figure 20: Cross–section schematic diagram of the DUV AlGaN MQW laser structure.

Figure 21 shows the rocking curve (ω–2θ scan) in (002) direction for sample 1-2643-1. The periodic fringe peaks, which contain information on the composition and the thickness of QWs and QBs, of the MQW structure is clearly shown. The existence of fringe peaks indicates that the sample has a smooth surface and has a relatively high–crystal quality. Simulation of the XRD data was performed and the results match the intended design very well. The surface morphology of the grown structure was measured by atomic–force microscopy (AFM) as shown in Fig.22. The well–developed steps, low defect density, and smooth surface were observed from these images. The corresponding RMS roughness for 5×5, 10×10, 20×20 μm^2 scan areas are 0.87, 0.90, and 0.91 nm, respectively.

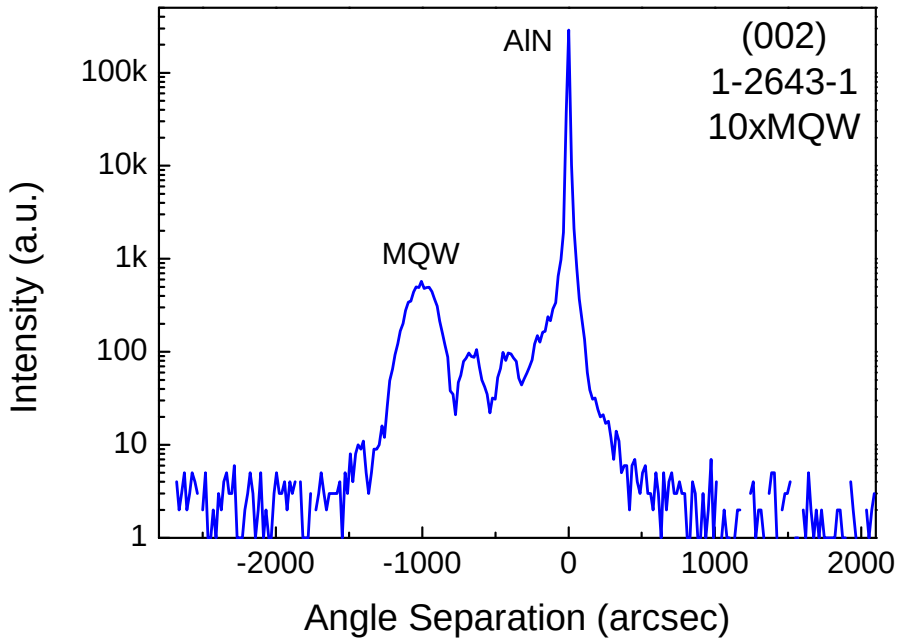

Figure 21: Rocking curve for 10×MQW structure grown on an AlN substrate. The two peaks between the AlN peak and the MQW peak are the fringes related to the AlGaN MQW peak, which indicates a high crystalline quality.

After the growth, the wafer was thinned to $\sim$ 80 μm by chemical–mechanical polishing of the back–side of the substrate. A Fabry–Perot etalon was formed by

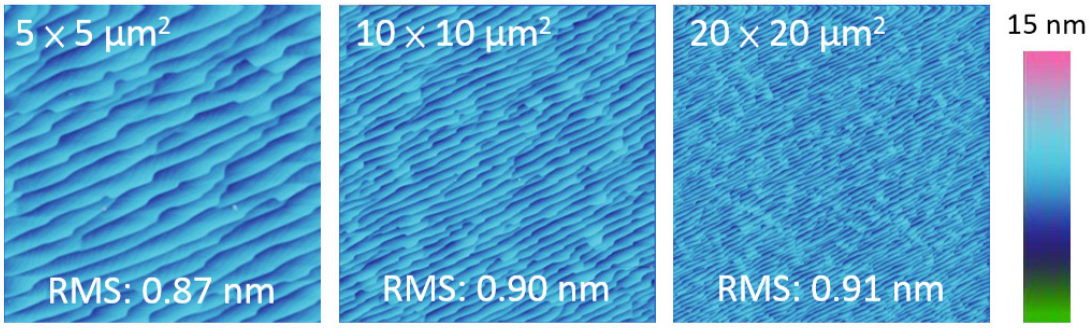

Figure 22: AFM measurements taken at 5×5, 10×10, 20×20 μm^2 and the corresponding RMS roughness values are 0.87, 0.90, and 0.91 nm, respectively.

cleaving along m–plane facets forming a cavity with a length of 1.25 mm. Figure 23 illustrates the optical pumping system used in this work. An ArF excimer laser (193 nm, $\hbar\omega \approx 6.42$ eV) running at a repetition rate of 10 Hz with a pulse width of 20 ns serves as the excitation source. The output of the laser passes through a series of steering mirrors and attenuators for power dependent measurements. At the exit of the attenuator, an optical aperture is used to shape the beam into a stripe shape, which is 1.27 cm in height and 0.1 cm in width. The beam is either reflected to a power meter for power density measurements or to illuminate the surface of laser bar. An optical fiber is placed in close proximity to the output facet of the laser bar to collect the emitted optical radiation. The far end of the fiber was connected to an Ocean Optics Maya 2000 Pro spectrometer ($\sim$ 0.1 nm resolution) by means of an SMA fitting. In order to obtain the polarization of the laser bar emission, a Glan–Laser α–BBO polarizer (100,000:1 extinction ratio) was inserted between the sample and the optical fiber.

The optical emission spectra recorded at room–temperature with various pumping power densities are described in Fig.24. The laser emission has a peak wavelength at 246.8 nm with a spectral linewidth reducing to 1.5 nm at the maximum measured

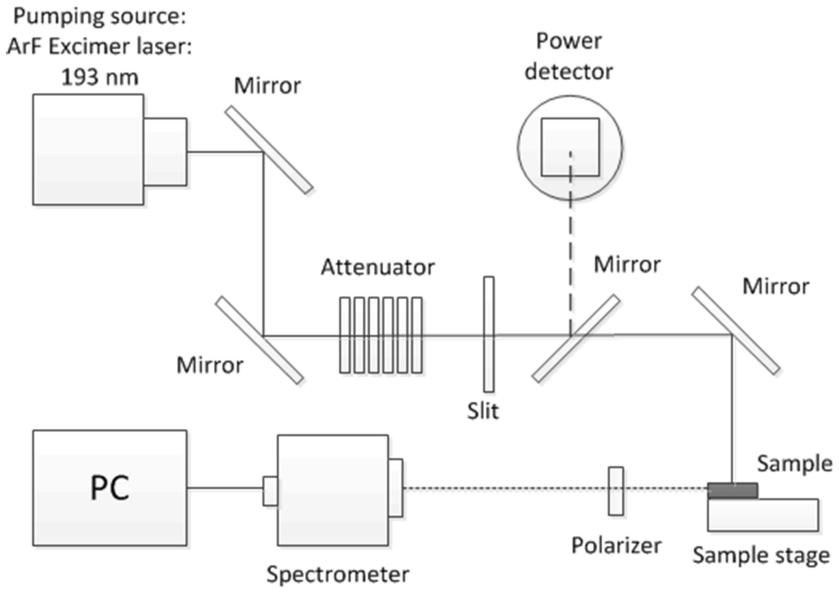

Figure 23: Schematic diagram of the experimental arrangement for the photoexcitation measurements.

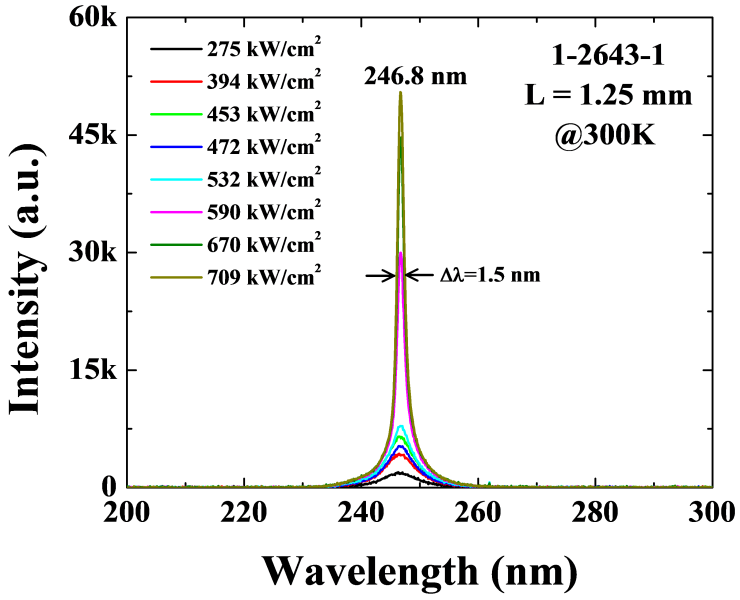

Figure 24: Optical emission spectra recorded at room temperature from an optically pumped laser bar from wafer 1-2643-1 under various excitation pumping power densities.

excitation power density of 709 kW/cm^2. In order to avoid any potential damage of the laser bar from the high energy laser pulses, measurement was limited to 1 MW/cm^2 pumping power density. Shown in Fig.25 is the optical output intensity as a function of excitation power density (L–L curve) and a distinct threshold power density (P_{th}) characteristic was observed at 445 kW/cm^2. The measured threshold power density is nearly three times lower than the previous reported optical–pumped UV laser grown on 4H–SiC with similar laser wavelength of 241.5 nm [42].

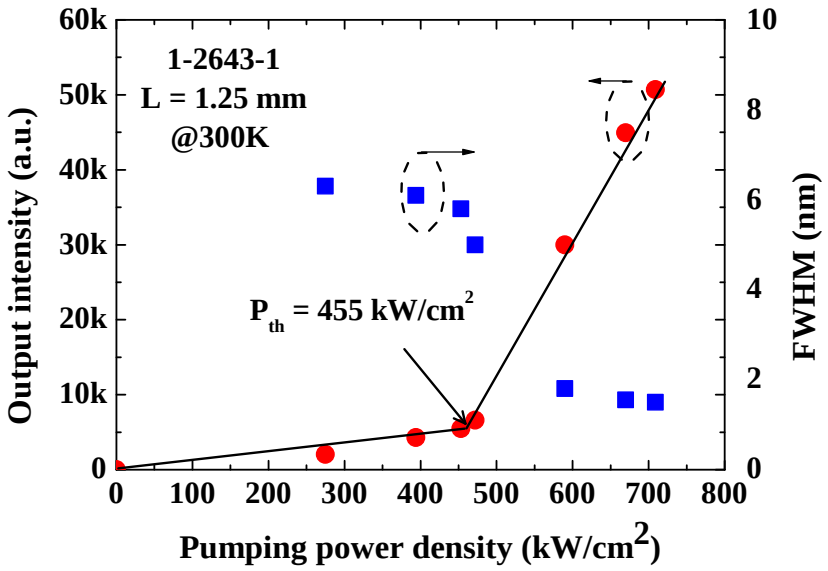

Figure 25: Laser bar emission and spectral linewidth as a function of pumping power density. The laser threshold is determined to be 455 kW/cm^2.

Emission spectra for transverse electric (TE) and transverse magnetic (TM) orientations are shown in Fig.26 for the cleaved laser bar from wafer 1-2643-1 grown on a bulk AlN substrate operating above threshold power density. Stimulated emission from the structure is strongly TE polarized with the degree of polarization (P) defined as

$$P = \frac{I_{TE} - I_{TM}}{I_{TE} + I_{TM}} = 91\% \tag{56}$$

For AlGaN ternary materials, the emission polarization switches from TE mode to TM mode as the aluminum molar fraction increases. The change in polarization is due to the change in valence band structure of AlGaN alloys. When the aluminum molar fraction increases, the crystal–field–split–off hole band becomes the top–most valence band instead of heavy hole (HH) band; therefore, the dominate recombination process becomes conduction band to crystal–field–split–off hole band, which has TM emission [43, 44]. Changes in band structure are induced when a sufficient compressive strain in the in–plane direction is applied to the AlGaN layer causes the dominate recombination process to become conduction band to HH band since the strain changes the top–most valence band from the crystal–field–split–off hole band

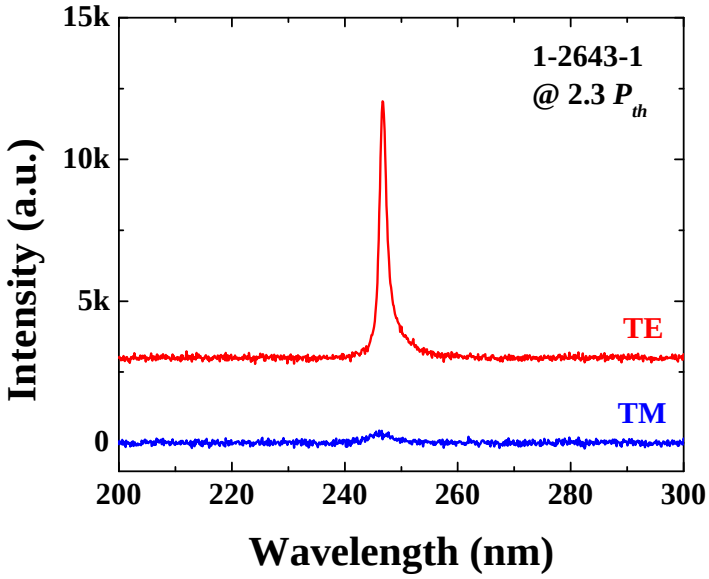

Figure 26: Optical emission spectra for both TE and TM polarizations recorded at room-temperature above threshold power density. An offset was applied to the TE emission spectra for visual clarity.

to HH band as described by Banal, et al. [45] and J. E. Northrup, et al. [46]. In this laser sample, the AlGaN MQW active region is grown on an AlN substrate, which results in the active region experiencing a significant strain in the in–plane direction; therefore, TE–dominated emission was observed. The measurements presented in this work along with those in related published work [47–49] indicate a similar conclusion that as sufficient strain is applied to the quantum wells, TE–mode gain continues to dominate into the DUV wavelengths.

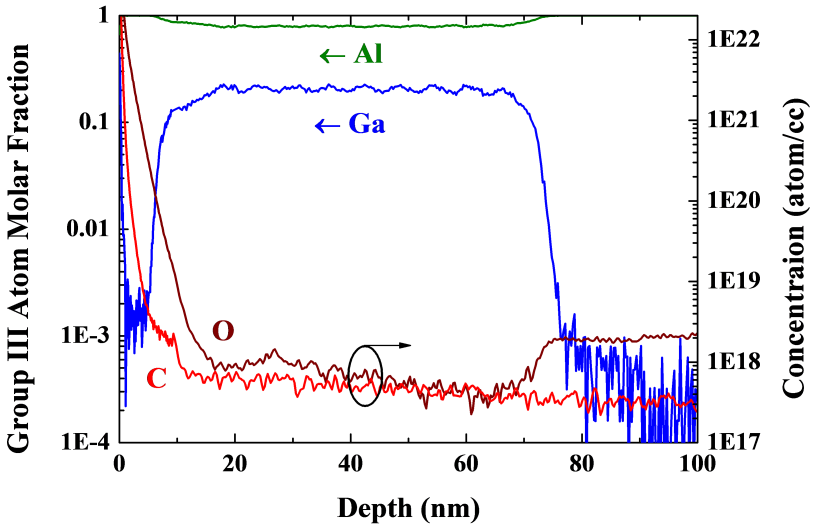

Figure 27: SIMS analysis of the optically pumped wafer. Low impurity concentrations were clearly shown; however, the last quantum well structure was not resolved.

Although this wafer successfully demonstrated low threshold optically pumped laser in the DUV wavelength range, SIMS data and HRTEM images suggest there are quantum wells that cannot be resolved. In addition, an aluminum rich mono–layer between wells and barriers is observed as well. Figure 27 shows the SIMS measurement data, low oxygen and carbon impurities in epitaxial layers is clearly shown. The molar fraction of gallium as function of depth shows nine periods of MQW structure while

the very last well was not observed. The HRTEM analysis on the active region of laser bar wafer along two different zone axes is shown in Fig.28. Both HRTEM images show only seven quantum wells; in addition, wells and barriers are separated by an aluminum rich mono–layer. The high aluminum molar fraction mono–layer can significantly affect the device performance as it may affect both electron and hole wavefunctions resulting a smaller overlap between the two carriers which further inhibits radiative recombination. Furthermore, the low contrast quantum well may serve as an absorption layer, which hampers the stimulated emission action. To solve these issues, the next laser bar is grown with a different technique, which will be discussed in detail in next section.

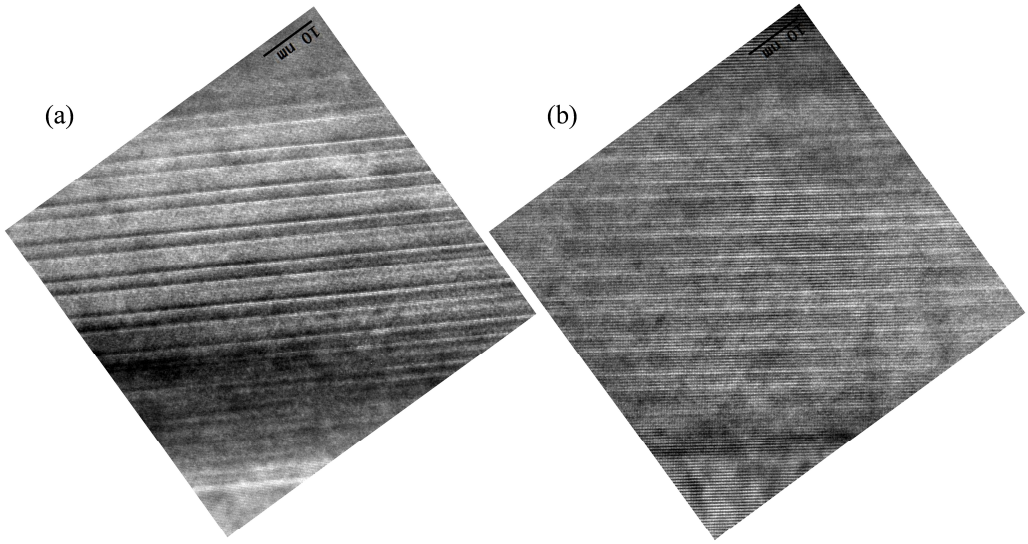

Figure 28: HRTEM images taken under (a) $(1\bar{1}00)$ zone axis and (b) $(11\bar{2}0)$ zone axis for the active region.

4.2.2 Sample 1-2651-5: 243.5 nm Optically Pumped DUV Laser

In order to create a more ideal MQW structure, a second TMGa source is introduced to achieve continuous growth between the wells and barriers. The advantage of using

a separate set of Ga sources for wells and barriers is to reduce the process time and a enable more stable source flow rate by employing constant Ga flow rate set points. More importantly, the SIMS analysis illustrated in Fig.29 clearly demonstrates the growth of the intended 10 uniform MQWs and STEM analysis in Fig.30 shows uniform quantum wells and that the unintentional aluminum–rich mono–layer is eliminated.

The atomic force microscope images illustrated in Fig.31 show terraced step–flow, which is the characteristic of two–dimensional layer–by–layer III–nitride epitaxial growth, indicating that a high crystalline quality is maintained with this continuous growth scheme. Figure 32 shows the high angle asymmetric (105) reciprocal spacing mapping (RSM) for wafer 1-2651-5. The perpendicular axis (Q_y) indicates the reciprocal lattice unit in the c direction while the horizontal axis (Q_x) indicates the reciprocal lattice unit in the in–plane lattice direction. All the epitaxial layers in

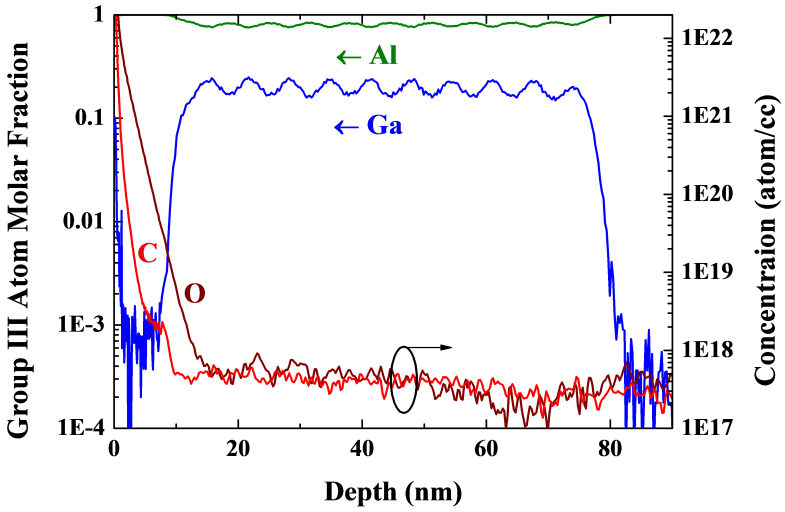

Figure 29: SIMS analysis of the optically pumped wafer 1-2651-5. Low impurity concentrations and 10 uniform quantum wells with high well and barrier contrast are clearly shown.

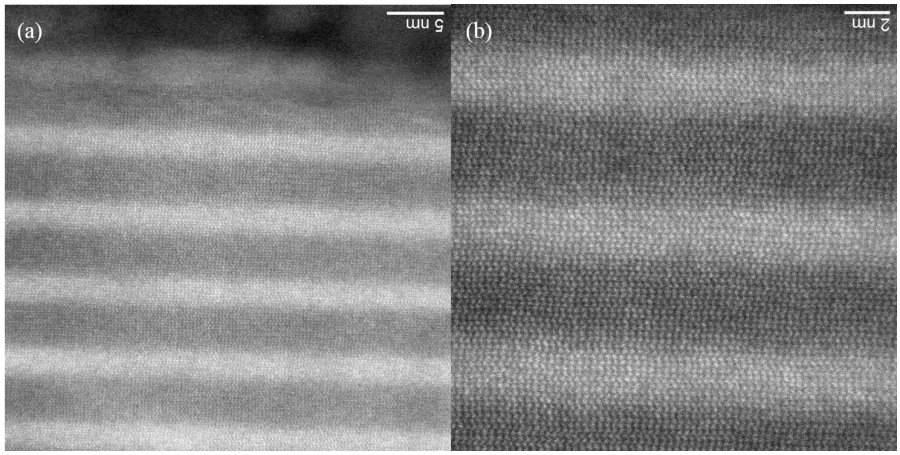

Figure 30: STEM images for (a) the active region of the 1-2651-5 optically pumped wafer and (b) at higher resolution.

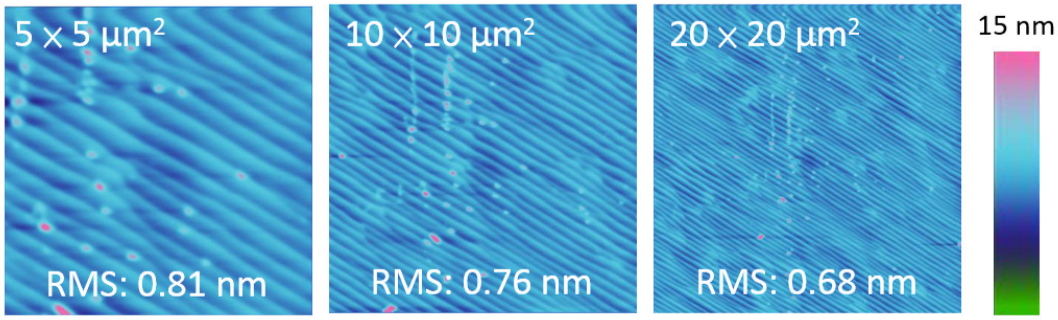

Figure 31: AFM measurements taken at 5×5, 10×10, 20×20 μm^2 and the corresponding RMS roughness values are 0.81, 0.76, and 0.68 nm, respectively.

sample 1-2651-5 are grown pseudomorphically as the in–plane lattice parameters are constant for the entire wafer and fully strained layers can inhibit the formation of the defects such as cracks and dislocations associated with lattice relaxation.

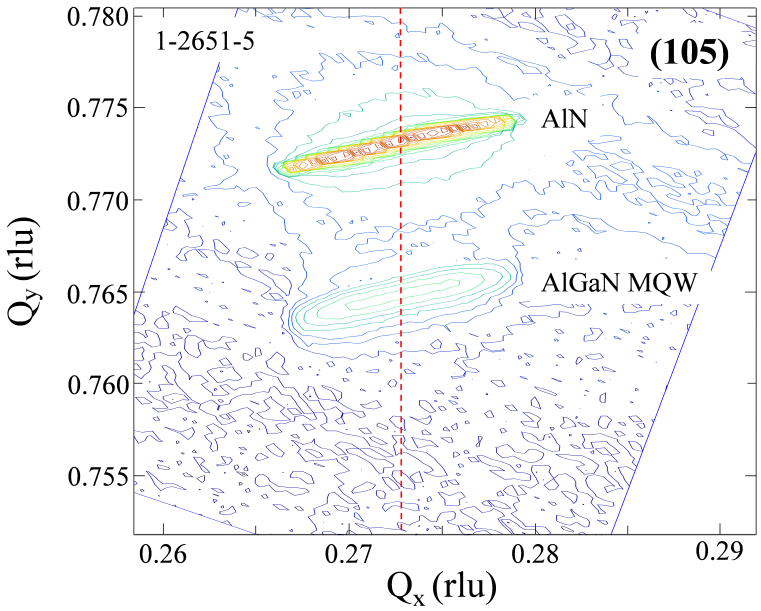

Figure 32: High angle asymmetric (105) RSM for wafer 1-2651-5. The in–plane lattice constant for both AlN buffer layer and active region are the same as shown by the vertical red dashed line, which indicates the epitaxial layers are grown pseudomorphically on the AlN substrate.

Identical optical excitation measurements as described in the previous section were performed again. Figure 33 shows the optical output spectra from the laser bar under various excitation pumping power densities at room–temperature. The peak emission wavelength is observed at 243.5 nm while the spectral linedwidth is reduced to 2.1 nm at the maximum measured pumping power density of 620 kW/cm^2. To determine the threshold pumping power density, L–L curve is shown in Fig.34 and the threshold pumping power density is determined to be 427 kW/cm^2. Compared to the previous laser sample, continuous growth scheme also provides a reduction in P_{th} by 28 kW/cm^2.

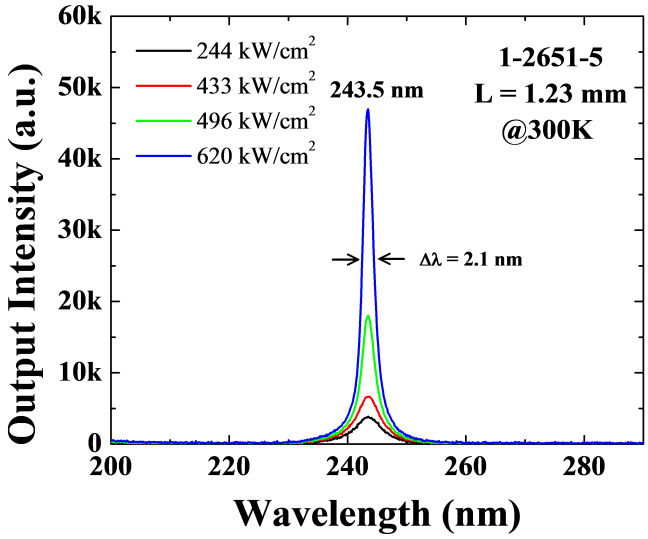

Figure 33: Optical emission spectra recorded at room temperature from 1-2651-5 optically pumped laser bar for various excitation pumping power densities.

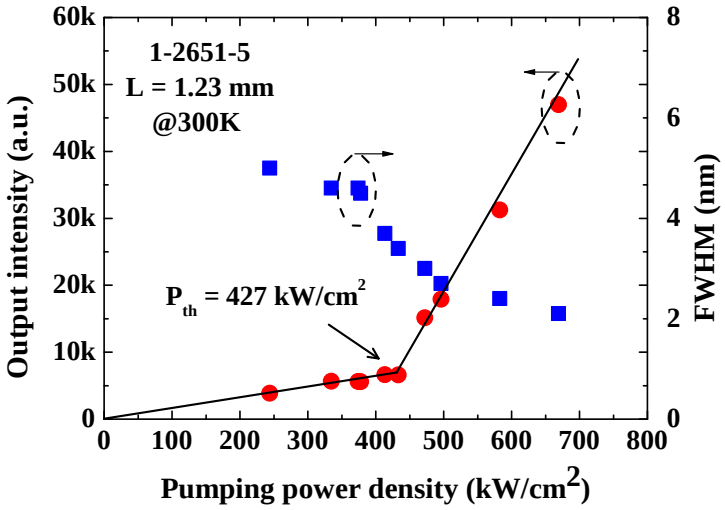

Figure 34: Laser bar emission and spectral linewidth as a function of pumping power density. The laser threshold is determined to be 427 kW/cm^2.

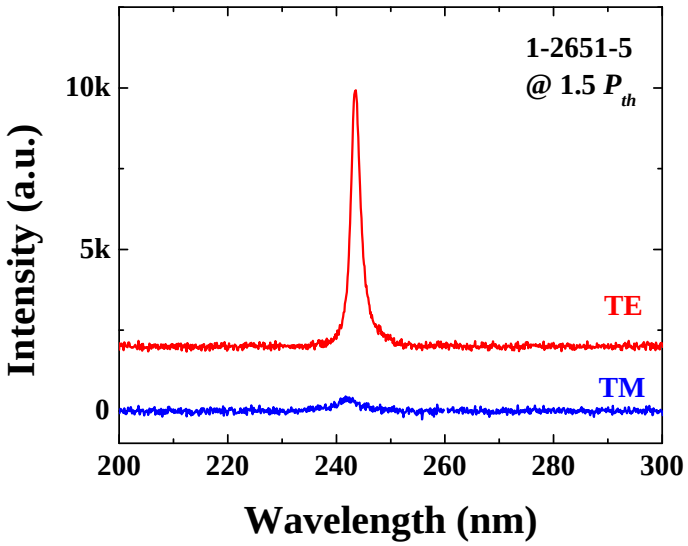

Figure 35: Optical emission spectra for both TE and TM polarizations recorded at room-temperature above threshold power density. An offset was applied to the TE emission spectra for visual clarity.

Emission spectra for both TE–like and TM–like emission from the cleaved laser bar operating above threshold power density ($\sim 1.5P_{th}$) are shown in Fig.35. The stimulated emission observed here is strongly TE–dominated emission again with the degree of polarization (P) about 91%. Strong TE–dominate emission with similar degree of polarization validates the prediction on the polarization is highly strain dependent [45, 46].

4.2.3 Sample 1-2693-2: 248.3 nm Optically Pumped DUV Laser

By introducing a continuous growth scheme for the laser active region, a more ideal MQW structure was achieved. In order to further reduce the threshold power density to a level such that laser action can be achieved by electrical injection, the structural design of the laser required further improvement. First of all, the AlN surface passivation layer is not transparent to the excitation laser, which reduces the amount of

excitation energy reaching the active region; therefore, the thickness of cap layer is reduced to 80% of original thickness. Furthermore, reduction in active region volume also reduces the threshold; therefore, the number of quantum wells is reduced 80% again i.e., 8 quantum wells instead of 10. When the total thickness of active region decreases, the optical confinement factor (Γ) decreases as well resulting in an increase in the threshold. In order to compensate for the reduction in the optical confinement factor, the quantum barrier thickness is increased by 20%; thus, the overall active region thickness is only slightly reduced by $\sim 7\%$.

This wafer was examined using material characterization as detailed previously, and high crystal–quality was measured by AFM as illustrated in Fig.36: a smooth surface is observed with very low root–mean–squared (RMS) roughness. Furthermore, RSM in the (105) diffraction shows that material is fully strained and MQW fringes are also observed, indicating excellent material quality and a smooth surface.

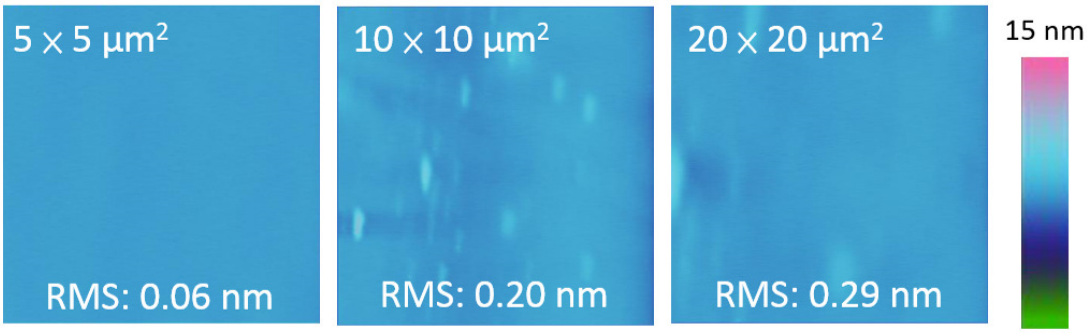

Figure 36: AFM measurements taken at 5×5, 10×10, 20×20 μm^2 and the corresponding RMS roughness values are 0.06, 0.20, and 0.29 nm, respectively.

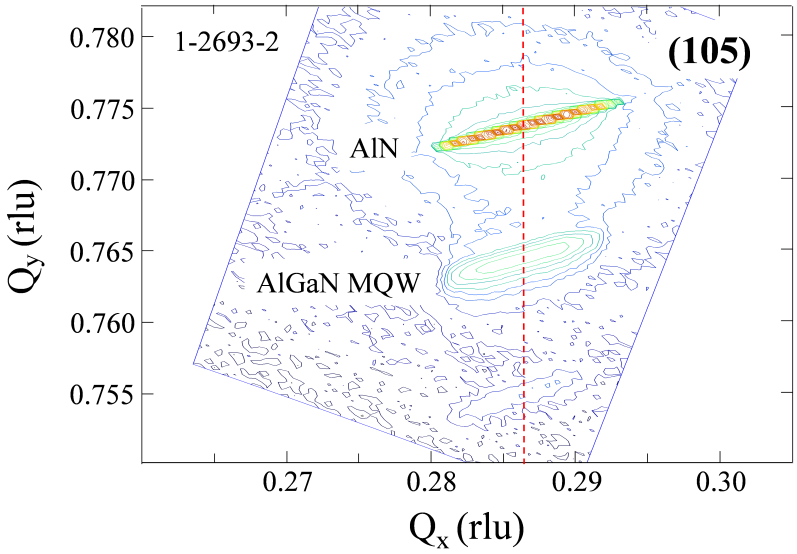

Figure 37: High angle asymmetric (105) RSM for wafer 1-2693-2. The epitaxial layers are grown pseudomorphically on an AlN substrate as the in–plane lattice constant is same for all the grown structure indicating by the red–dash line.

The material characterizations demonstrate the wafer has quality as good as previous samples; however, we observed a dramatic improvement in the laser performance. A 1.4 mm Fabry–Perot resonator was formed and the peak emission wavelength was observed at 248.3 nm with a linewidth of 0.8 nm, as per Fig.38. Furthermore, the threshold power density was determined to be 250 kW/cm^2 as shown in Fig.39, which corresponds to a $\sim$ 40% reduction in threshold power density compared to our previous best wafers. Since this sample has longer emission wavelength compared to the previous two, an even stronger degree of polarization is expected. Figure 40 illustrates the polarization measurement of this laser and a preferential TE–like emission was observed with the degree of polarization approaching 100 %. Further studies on this wafer by applying SiO_2/HfO_2 dielectric mirrors on both facets further reduced the

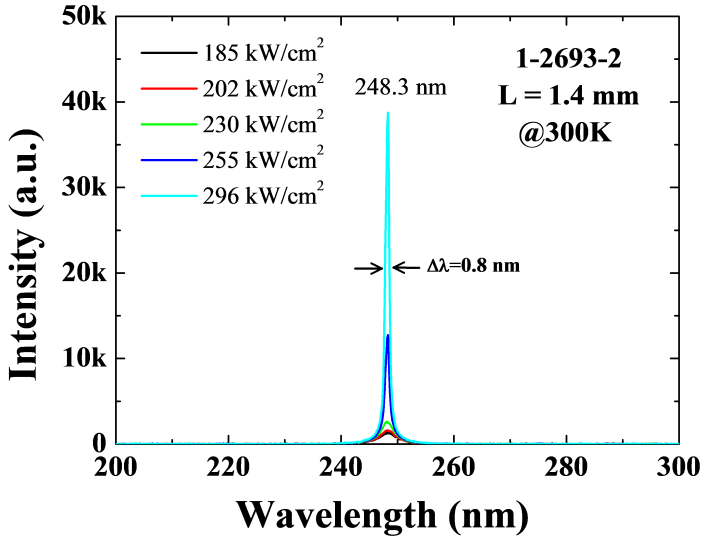

Figure 38: Optical emission spectra recorded at room temperature from the optically pumped laser bar 1-2693-2 under various excitation pumping power densities.

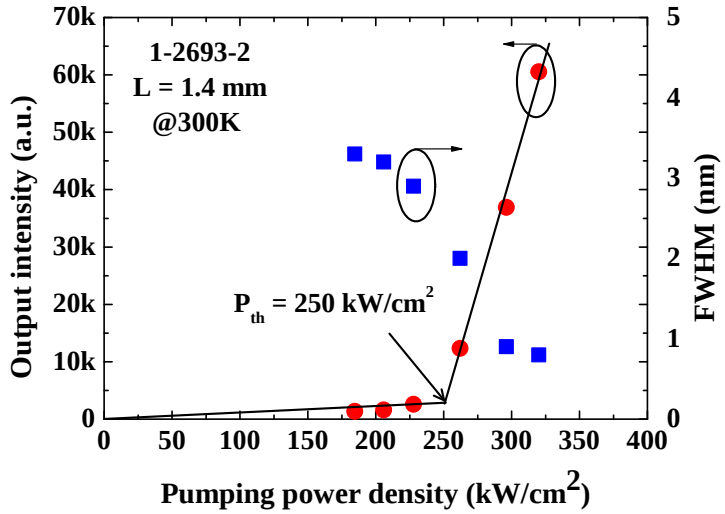

Figure 39: Laser bar emission and spectral linewidth as a function of pumping power density. Laser threshold is determined as 250 kW/cm^2.

threshold power density to 180 kW/cm^2. The internal loss (α_i) and threshold modal gain (G) can be calculated as 2 cm^{-1} and 10.9 cm^{-1}, respectively. The detail of this study is reported in Ref. [50].

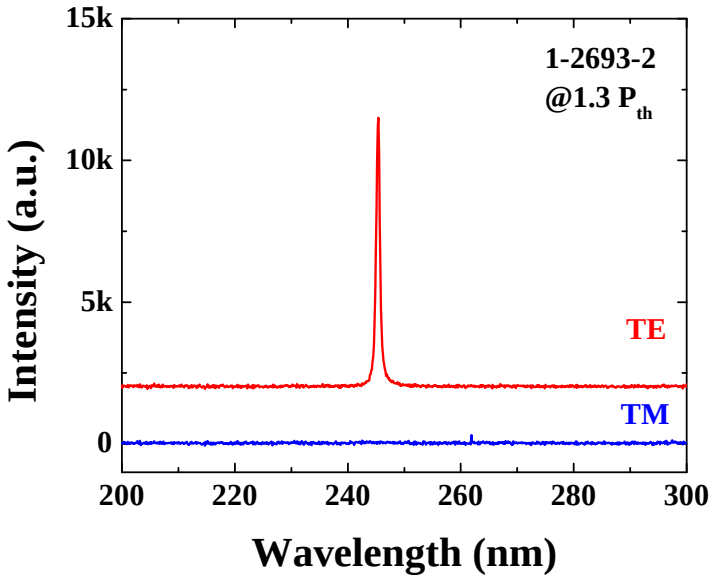

Figure 40: Optical emission spectra for both TE and TM polarizations recorded at room-temperature above threshold power density. An offset was applied to the TE emission spectra for visual clarity.

4.2.4 Optically Pumped DUV Laser Summary

Native AlN substrates were employed to demonstrate DUV optically pumped lasers. Growth on native substrates promote smooth surface formation as well as superior crystal quality. To improve the energy band profile of the active region, a continuous growth scheme between wells and barriers was achieved by utilizing two TMGa sources. To further reduce the threshold power density, the layer structure was further improved by reducing the active region volume and maintaining the optical confinement factor. From the improved layer structure design, a $\sim$ 40% reduction in threshold power density was observed. Polarization measurements on all the laser

samples exhibit a strong TE–dominate emission due to recombination process that is dominated by the conduction band to heavy hole transition when sufficient strain is applied on active region. By utilizing this observation, a diode laser can be designed to promote better optical confinement factor and further reducing threshold current density.

4.3 Ultraviolet Diode Emitter

4.3.1 Electrical Characteristics of Doped AlGaN Ternary Alloys

The achievements in the optical pumping experiments demonstrated the basic optical properties of these wide–bandgap ternary MQW heterostructures; however, another requirement for a diode emitter is to have electrically conducting layers. In the III–nitride based materials, dopants typically substitute on the group III atom site; therefore, group IV and group II atoms are the typically used as donor atoms and acceptor atoms, respectively. In this study, silicon is used as a donor atom while magnesium is used as an acceptor atom and the corresponding precursors are silane and Cp_2Mg, respectively.

The growth of silicon–doped (n–type) and magnesium–doped (p–type) AlGaN alloys with different aluminum molar fractions were explored which are required for our design of a complex laser diode structure. To ensure measurement accuracy, different electrical characterization methods were employed, including Hall measurements and circular transmission line measurements (CTLM). For electrical characterization, a 250 nm thick Si–doped AlGaN layers were grown on top of an un–doped graded buffer layer. The graded buffer was used to alleviate the polarization charge at the AlN and AlGaN interface.

Table 4 summarizes the optimized electrical characteristics for various n–type AlGaN layers, including the free electron concentration (n), electron mobility (μ), and bulk resistivity (ρ). Vanadium-based metal alloy stacks (V/Al/Ti/Au) were

employed to form Ohmic contacts for CTLM and Hall measurements. A significant increase in the bulk resistivity for AlGaN films with aluminum molar fraction above 60% was observed. In addition, once the aluminum molar fraction reaches $\sim$ 80%, the material becomes highly resistive. Similar observations in bulk n–type AlGaN resistivity were reported by Katsuno, et al. [51] and Nakarmi, et al. [52].

Table 4: Summary of electrical properties from n–type AlGaN.

Sample Description	n (cm^{-3})	μ (cm^2/V·s)	ρ(Ω·cm)
n–$Al_{0.8}Ga_{0.2}N$	2.7×10^{17}	4.608	5
n–$Al_{0.73}Ga_{0.27}N$	7.1×10^{17}	8.872	0.65
n–$Al_{0.6}Ga_{0.4}N$	8.9×10^{17}	12.7	0.52
n–$Al_{0.47}Ga_{0.53}N$	2.1×10^{18}	23.8	0.12

On the other hand, obtaining the electrical characteristics for p–type AlGaN is not trivial as Hall measurements and CTLM measurements require p–type Ohmic contacts, which are difficult to achieve. Due to the compliance limitations of our Hall measurement system, the resistivity of p–type AlGaN:Mg films is estimated by CTLM measurement when a 10V bias is applied across the pattern. Nickel–based metal alloy (Ni/Ag/Pt) was employed as metal contact and the estimated resistivity is summarized in Tab. 5.

Table 5: Summary of the electrical properties of p–type AlGaN.

Sample Description	ρ(Ω·cm)
p–$Al_{0.6}Ga_{0.4}N$	18.25
p–$Al_{0.47}Ga_{0.53}N$	8.75
p–$Al_{0.4}Ga_{0.6}N$	7.25

Since Hall measurements cannot be obtained accurately, the impurity concentrations were measured by secondary ion mass spectroscopy (SIMS) for p–AlGaN

samples. Two sets of measurements were performed to predict the doping concentrations for the wide spectrum of high aluminum p–AlGaN Mg–doped alloys. In the first set of measurement studies, the correlation between Cp_2Mg flow rate and the magnesium concentration in the layers is shown in Fig.41. The flow rates of Cp_2Mg were set to 600 sccm and 1000 sccm, or 2/3 of maximum flow, for the p–type $Al_{0.6}Ga_{0.4}N$ and the corresponding magnesium atomic concentrations are 1.2×10^{19} cm^{-3} and 2×10^{19} cm^{-3}, respectively. Based on the magnesium concentrations and source flow rates, every 100 sccm Cp_2Mg flow provides roughly 2×10^{18} cm^{-3} of magnesium concentration; therefore, doping concentrations as high as $\sim 3 \times 10^{19}$ cm^{-3} can be achieved under the given $Al_{0.6}Ga_{0.4}N$ growth conditions.

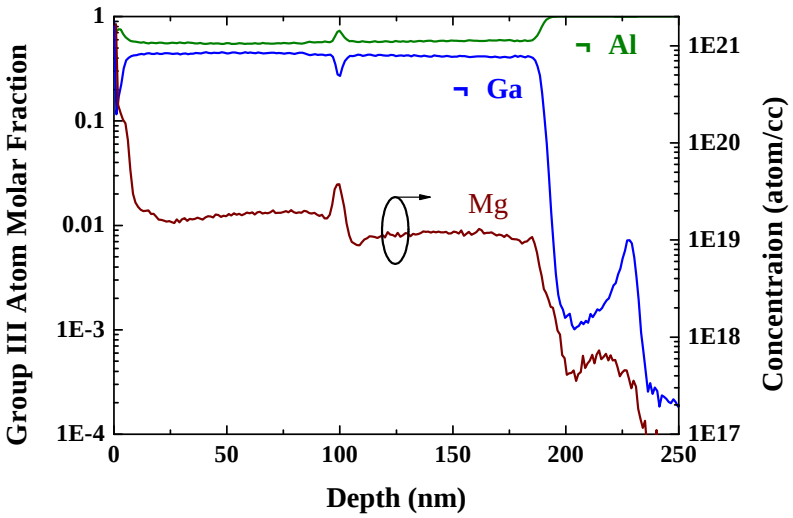

Figure 41: Secondary ion mass spectroscopy of a p–type $Al_{0.6}Ga_{0.4}N$ Mg–doped layer with two different Mg doping conditions.

Figure 42 shows SIMS data for AlGaN layers having various aluminum compositions grown at a constant magnesium source flow rate (1000 sccm). P–type ternary AlGaN alloys having three different aluminum molar fractions, 40%, 60%, and 80% were grown on top of AlN templates. Due to the difference in growth rate and V/III

ratio employed for different aluminum molar fractions, incorporation of magnesium varies. However, SIMS measurements suggest that a Mg doping concentration above 10^{19} cm^{-3} in most of the p–type AlGaN alloys can be achieved.

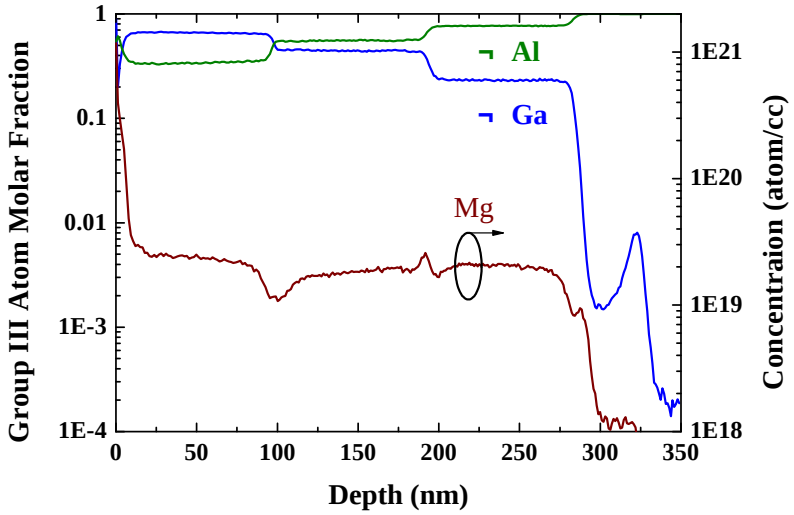

Figure 42: Secondary ion mass spectroscopy of Mg–doped p–type $Al_xGa_{1-x}N$ layers having different Al–compositions with a constant magnesium source flow.

4.3.2 Epitaxial Structure Design

In order to achieve a laser diode, a more complex epitaxial structure is required to transport carriers to the active region efficiently while maximizing the optical confinement. Figure 43 illustrates a schematic digram of a graded–index separate confinement heterostructure (GRINSCH) multi–quantum well (MQW) ridge waveguide ultraviolet emitter. The active region consists of a four–period MQW structure, with 2 nm $Al_{0.32}Ga_{0.68}N$ wells and 5 nm $Al_{0.47}Ga_{0.53}N$ barriers, which emits photons with a peak wavelength of ∼350 nm. Grading layers between the quantum barriers and the waveguide layers are employed to enhance carrier confinement as well as optical confinement.

To confine the optical mode in the transverse direction, a 500 nm thick n–type

$Al_{0.60}Ga_{0.40}N$ layer and a 400 nm thick p–type $Al_{0.60}Ga_{0.40}N$ layer served as waveguide layers. In addition to the optical confinement purpose, the n–type waveguide layer also serves as the contact layer and the metal contact consists of a vanadium–based metal alloy. Below the n–type contact/waveguide layer, a twelve–period short period superlattice (SPSL) with 4 nm $Al_{0.60}Ga_{0.40}N$ wells and 4 nm $Al_{0.73}Ga_{0.27}N$ barriers was used to enhance the lateral conduction and for strain relaxation management. Lastly, a n–type $Al_xGa_{1-x}N$ graded buffer layer with aluminum molar fraction varying from x = 1 to 0.73 is sandwiched between the AlN substrate and the SPSL to avoid an abrupt change in aluminum composition, which alleviates the polarization charge at the interface.

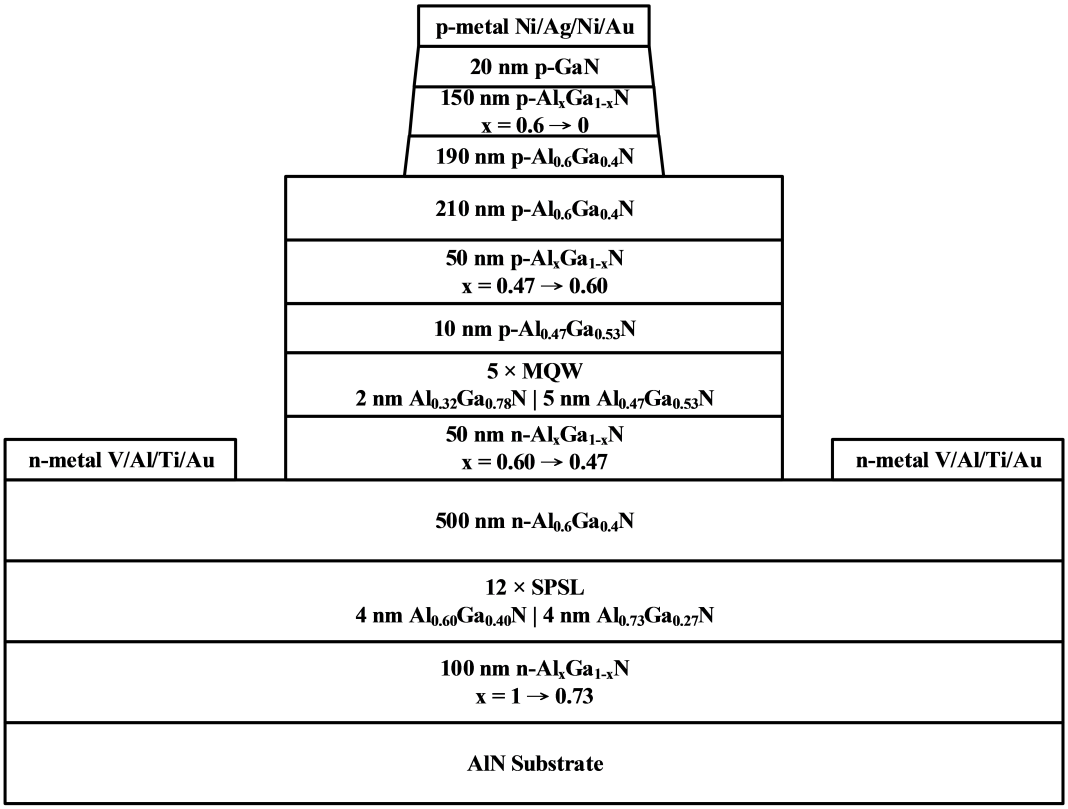

Figure 43: A schematic diagram of a deep–ultraviolet emitter.

Because nickel is a lossy material in the ultraviolet spectral range, it is necessary to position the p–Ohmic contact far away from the optical mode to reduce the optical

loss. In addition, the p–type contact layer needs to be deposited on a low aluminum molar fraction AlGaN or on GaN to avoid the formation of a Shottky contact. Therefore, an inversed tapered p–layer design, with the aluminum molar fraction graded from 0.6 to 0, is employed to bring the p–type metal contact away from the optical mode and form a flat valence band between the p–contact layer and the active region for efficient hole transportation [41]. The very last epitaxial layer for the laser structure is a 20 nm p–type GaN contact layer and the metal contact consists of a nickel–based metal alloy.

To form a ridge waveguide emitter, wafers underwent a series fabrication processes performed by our colleague, Louis Kao, in the Semiconductor Research Laboratory. Stripe–geometry ridge structures with various mesa widths (2–12 μm) were formed by inductively–coupled plasma reactive ion etch (ICP–RIE) process. To avoid etching damage, a more chemically driven etching process was performed; therefore, the ridge sidewalls were formed with an angle of $\sim$80° respect to the mesa. Once the ridge structure was formed for lateral confinement of optical mode, the n–contact layer mesa etch was then performed. To ensure smooth sidewalls for reducing leakage currents, photoelectrochemical (PEC) etching of the mesa sidewalls was performed with a 150 W Xe arc lamp. Metal alloy stacks of V/Al/Ti/Au with thickness of $300\mathring{A}/500\mathring{A}/300\mathring{A}/500\mathring{A}$, for n–type metal contact was deposited by an e–beam evaporator and annealed in a nitrogen ambient at 450°C for ten minutes and 850°C for 30 seconds. Next, a p–type metal alloy, Ni/Ag/Ni/Au with thickness of $30\mathring{A}/1000\mathring{A}/200\mathring{A}/200\mathring{A}$, was deposited and annealed in compressed air at 450°C for two minutes. Surface passivation using spin–on–glass (SOG) was performed to enhance both electrical and optical confinement of emitter.

4.3.3 Device Characterizations

Once the device was fabricated, a series of electrical and optical characterizations was performed. Figure 44 illustrates the transmission line measurement (TLM) for both p–contact and n–contacts. Schottky barriers were observed with potential barrier heights of ∼0.5 V and ∼1 V for the p–contact and n–contact, respectively. This non–Ohmic behavior for the metal contacts contribute an additional parasitic resistance and results in a relatively large turn on voltage (V_{on}), which will be described in detail. Although Ohmic contacts weren't successfully formed, the sheet resistance (R_{sh}) can still be estimated by measuring the total resistance at the bias above the Schottky barrier height. Utilizing the total resistance measured at 5V, R_{sh} for the p–contact and n–contact layers were estimated to be 167 kΩ/□ and 233 Ω/□, respectively.

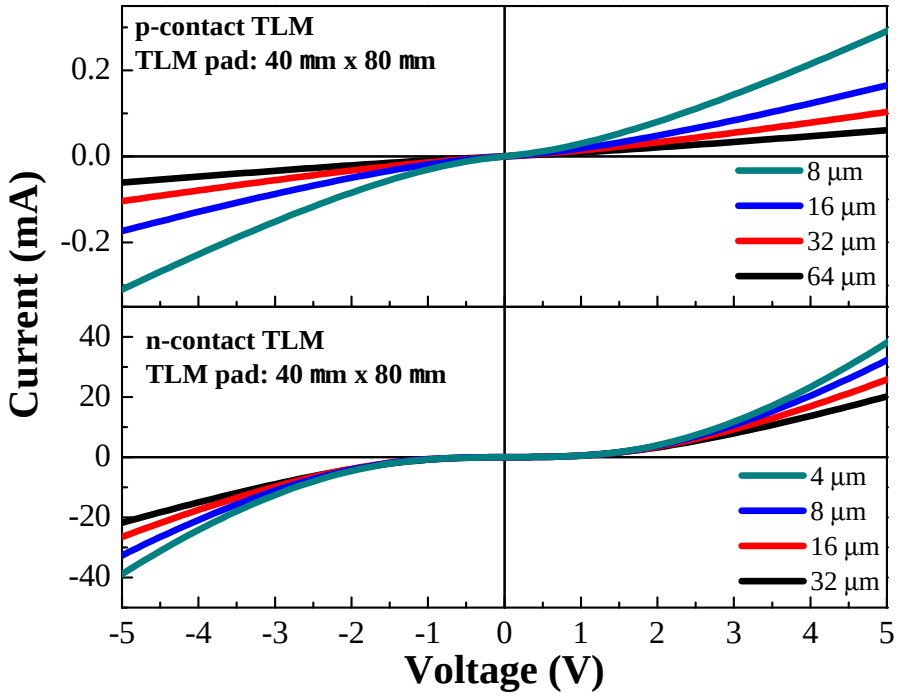

Figure 44: Transmission line measurement for p–contact (top panel) and n–contact (bottom panel).

The current–voltage (I–V) measurement for the diode being operated under DC

condition is illustrated in Fig.45. The turn on voltage for the calibration sample grown on sapphire is determined to be ∼7V for both n–type and p–type Ohmic contacts; however, the turn on voltage is measured to be ∼ 9V for the sample grown on an AlN substrate and the difference may originate from the Schottky barriers observed from the metal–semiconductor junctions. Under D.C. forward bias, the device sustained a current level of at least 225 mA, which is equivalent to a current density of ∼ 10kA/cm^2 and the series resistance at this current density is measured as ∼ 15Ω. The current density achieved in this work is comparable to the value of reported previously 11 kA/cm^2 [53]; however, the thickness of the waveguide layer is more than two times larger than the reported value, which indicates that the inverse tapering is another solution for efficient vertical hole transport in high aluminum–containing AlGaN.

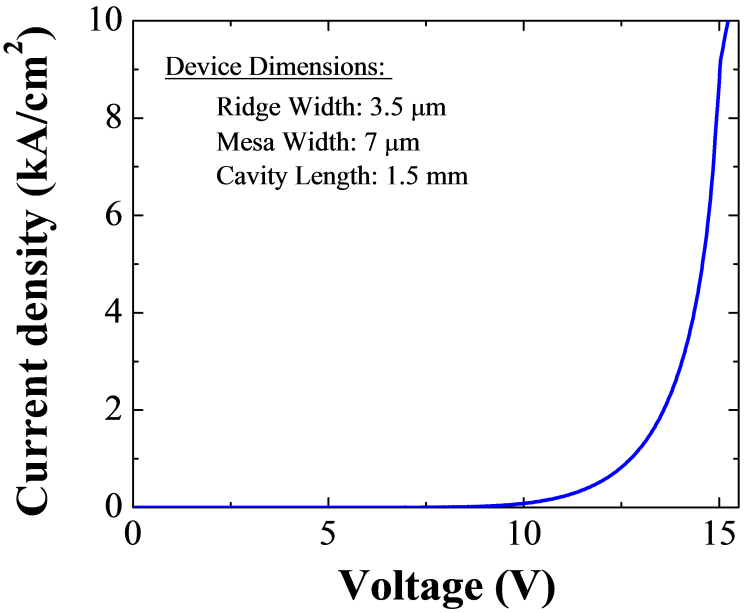

Figure 45: Current–voltage measurement of a graded–index separate confinement heterostructure device with inverse tapered p–layer under DC operation.

Figure 46 illustrates the electroluminescence (EL) spectra of the ultraviolet emitter

operating in pulse mode at room temperature (RT). The current pulse has a pulse width of 1μs while the pulsing frequency is set as 5kHz. The peak emission wavelength was determined to be at $\sim$ 350 nm while the spectral linewidth narrowed from $\sim$ 71 nm to $\sim$ 64 nm. The relatively wide spectral linewidth may originate from the insufficient net capture rate in active region or polishing damage on AlN surface, which provides a rough surface and results mixing of the epitaxial layers. Although laser action wasn't successfully achieved, the demonstration of a highly electrically conducting wide bandgap AlGaN diode confirms the viability of the inverse tapering design for future development of DUV laser diodes.

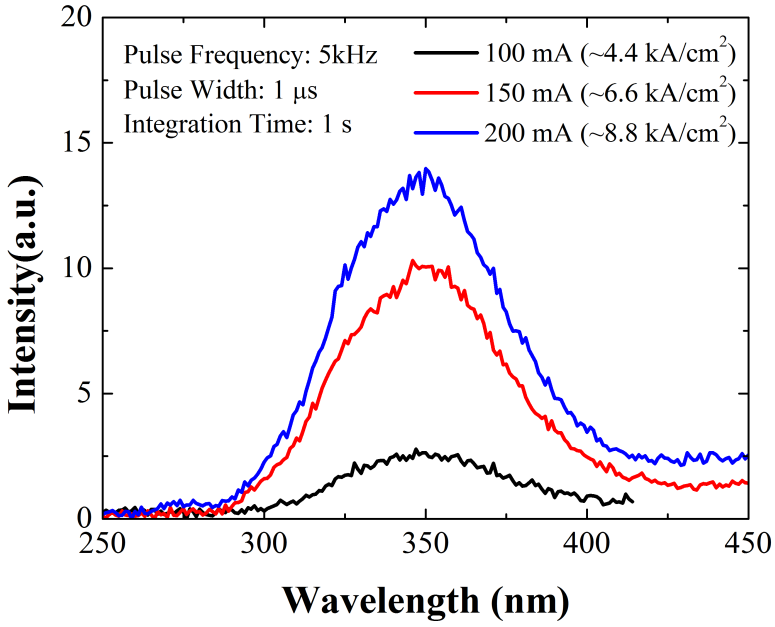

Figure 46: Electroluminescence spectra at 300K of an AlGaN MQW ultraviolet emitter grown on an AlN substrate operating in continuous wave.

CHAPTER V

SUMMARY

Deep–ultraviolet (DUV) emitters grown by metalorganic chemical vapor deposition (MOCVD) were demonstrated. The aluminum gallium nitride (AlGaN) ternary alloy material system was selected to use for these DUV emitters growth owing to the direct– and wide–bandgap structure of this III–N ternary alloy. In addition, the superior thermal conductivity of AlN not only facilitates uniform epitaxial growth, but also inhibits Joule heating during the operation of the devices. A 6 × 2" Thomas Swan (now AIXTRON) MOCVD closed–coupled showerhead reactor with a LayTec in–situ monitoring system was employed to perform epitaxial growth. Various material characterization techniques employed in this thesis research, including atomic–force microscopy (AFM), electroluminescence (EL), Hall–effect measurement, photoluminescence (PL), secondary ion mass spectrometry (SIMS), transmission electron microscopy (TEM), transmission–line measurement (TLM), and X–ray diffraction (XRD), were discussed.

Various optically pumped sub–250 nm lasers grown on AlN substrates operating at room temperature were described. Laser operation of AlGaN MQW heterostructures were observed by employing an ArF (λ = 193 nm) excimer laser as the excitation source to generate electron–hole pairs in the active region, which consists of an AlGaN–based multi–quantum well (MQW) structure. The peak emission wavelength for the first optically pumped laser was observed at 246.8 nm with a threshold power density of 455 kW/cm^2 [54]. This result confirmed the viability of AlN substrates for future development of DUV AlGaN–based laser diodes; however, an aluminum rich mono–layer was observed at quantum well and quantum barrier interface by high

angle annular dark field (HAADF) analysis.

To form a more ideal quantum–well band structure, a second trimethylgallium (TMGa) source was introduced to achieve a continuous growth scheme between the quantum wells and the quantum barriers. The analysis from HAADF measurements showed the continuous growth scheme successfully eliminated the aluminum rich mono–layer. The peak wavelength for this optically pumped laser was at 243.5 nm with a threshold power density of 427 kW/cm^2 [55]. Although this laser bar successfully created a more ideal quantum–well structure, the threshold power density is still relatively high for a laser diode.

In order to further reduce the threshold pumping power density, the layer structure was optimized by reducing the active region volume and the thickness of surface passivation layer. To compensate for the reduction in optical confinement originating from reducing the number of quantum wells, thicker quantum barriers were employed. A threshold power density as low as 250 kW/cm^2 was achieved. Furthermore, polarization studies on these optically pumped laser shows strong transverse electric (TE) –dominate emission, suggesting the layer structure design must be optimized such that the active region is still experiences sufficient compressive strain in the in–plane direction to promote better optical confinement factor.

In an effort to demonstrate electrical devices, various doping conditions for n–type and p–type wide–bandgap AlGaN ternary alloys were explored. Highly conducting AlGaN ternary layers can be achieved with silicon and magnesium doping in a wide range of aluminum molar fractions. Utilizing these doping conditions, a ridge waveguide graded–index separate confinement heterostructure (GRINSCH) MQW ultraviolet emitter was demonstrated. The devices can sustain a forward current density of at least $\sim$10kA/cm^2 before break down under DC measurement conditions. Although laser action wasn't successfully demonstrated, the demonstration of electrical performance suggests the inverse tapered design for efficient hole transporting may

be a potential avenue to achieve DUV laser diodes (LDs).

Future development of DUV LDs will highly depend on the p–type doping technology as these p–type alloys are relatively resistive, which limits the degree of freedom in structural design. Other approaches to alleviate the difficulty in designing p–layers include novel p–type Ohmic contacts, novel p–type dopants, and an improved activation scheme. In addition to the growth technology, the quality of AlN native substrates is another limiting factor as the defect density is still relatively high and immature polishing technology significantly affects the device performance as well as the surface morphology of grown layers, respectively. Further improvement in electrical characteristics while maintaining optical confinement will be the next step toward the realization in DUV LDs.

REFERENCES

[1] R. N. Hall, G. E. Fenner, J. D. Kingsley, T. J. Soltys, and R. O. Carlson, "Coherent Light Emission From GaAs Junctions," *Phys. Rev. Lett.*, vol. 9, pp. 366–368, Nov 1962.

[2] M. I. Nathan, W. P. Dumke, G. Burns, J. Frederick H. Dill, and G. Lasher, "STIMULATED EMISSION OF RADIATION FROM GaAs p-n JUNCTIONS," *Applied Physics Letters*, vol. 1, no. 3, pp. 62–64, 1962.

[3] N. Holonyak and S. F. Bevacqua, "COHERENT (VISIBLE) LIGHT EMISSION FROM $Ga(As_{1-x}P_x)$ JUNCTIONS," *Applied Physics Letters*, vol. 1, no. 4, pp. 82–83, 1962.

[4] T. M. Quist, R. H. Rediker, R. J. Keyes, W. E. Krag, B. Lax, A. L. McWhorter, and H. J. Zeigler, "SEMICONDUCTOR MASER OF GaAs," *Applied Physics Letters*, vol. 1, no. 4, pp. 91–92, 1962.

[5] S. Nakamura, M. Senoh, S. ichi Nagahama, N. Iwasa, T. Yamada, T. Matsushita, H. Kiyoku, and Y. Sugimoto, "InGaN-Based Multi-Quantum-Well-Structure Laser Diodes," *Japanese Journal of Applied Physics*, vol. 35, no. Part 2, No. 1B, pp. L74–L76, 1996.

[6] Y. C. Cheng, X. L. Wu, J. Zhu, L. L. Xu, S. H. Li, and P. K. Chu, "Optical properties of rocksalt and zinc blende AlN phases: First-principles calculations," *Journal of Applied Physics*, vol. 103, no. 7, p. 073707, 2008.

[7] T. Hashimoto, K. Fujito, R. Sharma, E. R. Letts, P. T. Fini, J. S. Speck, and S. Nakamura, ""Phase selection of microcrystalline GaN synthesized in supercritical ammonia," *Journal of Crystal Growth*, vol. 291, no. 1, pp. 100 – 106, 2006.

[8] S. R. Lee, A. F. Wright, M. H. Crawford, G. A. Petersen, J. Han, and R. M. Biefeld, "The band-gap bowing of $Al_xGa_{1-x}N$ alloys," *Applied Physics Letters*, vol. 74, no. 22, pp. 3344–3346, 1999.

[9] Q. S. Paduano, D. W. Weyburne, L. O. Bouthillette, S.-Q. Wang, and M. N. Alexander, "The Energy Band Gap of $Al_xGa_{1-x}N$," *Japanese Journal of Applied Physics*, vol. 41, no. Part 1, No. 4A, pp. 1936–1940, 2002.

[10] W. Shan, J. W. A. III, K. M. Yu, W. Walukiewicz, E. E. Haller, M. C. Martin, W. R. McKinney, and W. Yang, "Dependence of the fundamental band gap of $Al_xGa_{1-x}N$ on alloy composition and pressure," *Journal of Applied Physics*, vol. 85, no. 12, pp. 8505–8507, 1999.

[11] J. Wu, W. Walukiewicz, K. M. Yu, J. W. A. III, E. E. Haller, H. Lu, and W. J. Schaff, "Small band gap bowing in $In_{1-x}Ga_xN$ alloys," *Applied Physics Letters*, vol. 80, no. 25, pp. 4741–4743, 2002.

[12] "Optical properties and electronic structure of InN and In-rich group III-nitride alloys," *Journal of Crystal Growth*, vol. 269, no. 1, pp. 119 – 127, 2004.

[13] A. E. Romanov, T. J. Baker, S. Nakamura, J. S. Speck, and E. U. Group, "Strain-induced polarization in wurtzite III-nitride semipolar layers," *Journal of Applied Physics*, vol. 100, no. 2, p. 023522, 2006.

[14] M. Suzuki and T. Uenoyama, " Biaxial Strain Effect on Wurtzite GaN/AlGaN Quantum Well Lasers," *Japanese Journal of Applied Physics*, vol. 35, no. Part 1, No. 2B, pp. 1420–1423, 1996.

[15] S. L. Chuang and C. S. Chang, "A band–structure model of strained quantum–well wurtzite semiconductors," *Semiconductor Science and Technology*, vol. 12, no. 3, p. 252, 1997.

[16] H. Morkoç, S. Strite, G. B. Gao, M. E. Lin, B. Sverdlov, and M. Burns, "Large-band-gap SiC, III-V nitride, and II-VI ZnSe-based semiconductor device technologies," *Journal of Applied Physics*, vol. 76, no. 3, pp. 1363–1398, 1994.

[17] I. Vurgaftman and J. R. Meyer, "Band parameters for nitrogen–containing semiconductors," *Journal of Applied Physics*, vol. 94, no. 6, pp. 3675–3696, 2003.

[18] H. M. Manasevit, "SINGLE-CRYSTAL GALLIUM ARSENIDE ON INSULATING SUBSTRATES," *Applied Physics Letters*, vol. 12, no. 4, pp. 156–159, 1968.

[19] A. Cho and J. Arthur, "Molecular beam epitaxy," *Progress in Solid State Chemistry*, vol. 10, Part 3, no. 0, pp. 157 – 191, 1975.

[20] H. M. Manasevit and W. I. Simpson, "The use of metal-organics in the preparation of semiconductor materials," *Journal of The Electrochemical Society*, vol. 116, pp. 623 – 629, 1984.

[21] R. D. Dupuis, P. D. Dapkus, R. D. Yingling, and L. A. Moudy, "High–efficiency GaAlAs/GaAs heterostructure solar cells grown by metalorganic chemical vapor deposition," *Applied Physics Letters*, vol. 31, no. 3, pp. 201–203, 1977.

[22] R. D. Dupuis, P. D. Dapkus, J. Nick Holonyak, E. A. Rezek, and R. Chin, "Room–temperature laser operation of quantum-well $Ga_{1-x}Al_xAs$–GaAs laser diodes grown by metalorganic chemical vapor deposition," *Applied Physics Letters*, vol. 32, no. 5, pp. 295–297, 1978.

[23] G. Binnig and H. Rohrer, "Scanning tunneling microscopy," *IBM J. Res. Dev.*, vol. 44, pp. 279–293, Jan. 2000.

[24] G. Binnig, C. F. Quate, and C. Gerber, "Atomic Force Microscope," *Phys. Rev. Lett.*, vol. 56, pp. 930–933, Mar 1986.

[25] L. J. van der Pauw, "A Method of Measuring Specific Resistivity and Hall Effect of Discs of Arbitrary Shapes," *Philips Research Reports*, vol. 13, pp. 1–9, 1958.

[26] L. J. van der Pauw, "A Method of Measuring the Resistivity and Hall Coefficient on Lamellae of Arbitrary Shape," *Philips Technical Review*, vol. 20, pp. 220–224, 1958.

[27] S. Nakamura, N. Iwasa, M. Senoh, and T. Mukai, "Hole Compensation Mechanism of P-Type GaN Films," *Japanese Journal of Applied Physics*, vol. 31, no. Part 1, No. 5A, pp. 1258–1266, 1992.

[28] H. Amano, M. Kito, K. Hiramatsu, and I. Akasaki, "P-Type Conduction in Mg-Doped GaN Treated with Low-Energy Electron Beam Irradiation (LEEBI)," *Japanese Journal of Applied Physics*, vol. 28, no. Part 2, No. 12, pp. L2112–L2114, 1989.

[29] S. Nakamura, T. Mukai, M. Senoh, and N. Iwasa, "Thermal Annealing Effects on P-Type Mg-Doped GaN Films," *Japanese Journal of Applied Physics*, vol. 31, no. Part 2, No. 2B, pp. L139–L142, 1992.

[30] M. Knoll and E. Ruska, "Das elektronenmikroskop," *Zeitschrift für Physik*, vol. 78, no. 5-6, pp. 318–339, 1932.

[31] G. S. Marlow and M. B. Das, "The effects of contact size and non-zero metal resistance on the determination of specific contact resistance," *Solid-State Electronics*, vol. 25, no. 2, pp. 91 – 94, 1982.

[32] M. A. Moram and M. E. Vickers, "X-ray diffraction of iii-nitrides," *Reports on Progress in Physics*, vol. 72, no. 3, p. 036502, 2009.

[33] P. F. Fewster and N. L. Andrew, "Strain analysis by x-ray diffraction," *Thin Solid Films*, vol. 319, no. 12, pp. 1 – 8, 1998.

[34] O. Ambacher, J. Majewski, C. Miskys, A. Link, M. Hermann, M. Eickhoff, M. Stutzmann, F. Bernardini, V. Fiorentini, V. Tilak, B. Schaff, and L. F. Eastman, "Pyroelectric properties of Al(In)GaN/GaN hetero- and quantum well structures," *Journal of Physics: Condensed Matter*, vol. 14, no. 13, p. 3399, 2002.

[35] V. Fiorentini, F. Bernardini, F. Della Sala, A. Di Carlo, and P. Lugli, "Effects of macroscopic polarization in III–V nitride multiple quantum wells," *Phys. Rev. B*, vol. 60, pp. 8849–8858, Sep 1999.

[36] R. Kajitani, K. Kawasaki, and M. Takeuchi, "Barrier-height and well-width dependence of photoluminescence from AlGaN-based quantum well structures for deep–UV emitters ," *Materials Science and Engineering: B*, vol. 139, no. 23, pp. 186 – 191, 2007.

[37] M. Satter, Z. Lochner, J.-H. Ryou, S.-C. Shen, R. D. Dupuis, and P. Yoder, "Polarization Matching in AlGaN-Based Multiple-Quantum-Well Deep Ultraviolet Laser Diodes on AlN Substrates Using Quaternary AlInGaN Barriers," *Lightwave Technology, Journal of*, vol. 30, no. 18, pp. 3017–3025, 2012.

[38] H. Amano, N. Sawaki, I. Akasaki, and Y. Toyoda, "Metalorganic vapor phase epitaxial growth of a high quality GaN film using an AlN buffer layer," *Applied Physics Letters*, vol. 48, no. 5, pp. 353–355, 1986.

[39] A. Rice, R. Collazo, J. Tweedie, R. Dalmau, S. Mita, J. Xie, and Z. Sitar, "Surface preparation and homoepitaxial deposition of AlN on (0001)-oriented AlN substrates by metalorganic chemical vapor deposition," *Journal of Applied Physics*, vol. 108, no. 4, p. 043510, 2010.

[40] H. J. Kim, S. Choi, D. Yoo, J.-H. Ryou, R. D. Dupuis, R. F. Dalmau, P. Lu, and Z. Sitar, "Modulated precursor flow epitaxial growth of AlN layers on native AlN substrates by metal-organic chemical vapor deposition," *Applied Physics Letters*, vol. 93, no. 2, p. 022103, 2008.

[41] M. M. Satter, Z. Lochner, T.-T. Kao, Y.-S. Liu, , X.-H. Li, S.-C. Shen, R. Dupuis, and P. D. Yoder, "AlGaN-Based Vertical Injection Laser Diodes using Inverse Tapered P-waveguide for Efficient Hole Transport," *Submitted to IEEE J. Quantum Electronics*, 2013.

[42] T. Takano, Y. Narita, A. Horiuchi, and H. Kawanishi, "Room-temperature deep-ultraviolet lasing at 241.5 nm of AlGaN multiple-quantum-well laser," *Applied Physics Letters*, vol. 84, no. 18, pp. 3567–3569, 2004.

[43] H. Kawanishi, M. Senuma, and T. Nukui, "Anisotropic polarization characteristics of lasing and spontaneous surface and edge emissions from deep-ultraviolet ($\lambda \approx 240$ nm) AlGaN multiple-quantum-well lasers," *Applied Physics Letters*, vol. 89, no. 4, p. 041126, 2006.

[44] K. B. Nam, J. Li, M. L. Nakarmi, J. Y. Lin, and H. X. Jiang, "Unique optical properties of AlGaN alloys and related ultraviolet emitters," *Applied Physics Letters*, vol. 84, no. 25, pp. 5264–5266, 2004.

[45] R. G. Banal, M. Funato, and Y. Kawakami, "Optical anisotropy in [0001]-oriented $Al_xGa_{1-x}N$/AlN quantum wells (x>0.69)," *Phys. Rev. B*, vol. 79, p. 121308, Mar 2009.

[46] J. E. Northrup, C. L. Chua, Z. Yang, T. Wunderer, M. Kneissl, N. M. Johnson, and T. Kolbe, "Effect of strain and barrier composition on the polarization of light emission from AlGaN/AlN quantum wells," *Applied Physics Letters*, vol. 100, no. 2, p. 021101, 2012.

[47] T. Wunderer, C. L. Chua, J. E. Northrup, Z. Yang, N. M. Johnson, M. Kneissl, G. A. Garrett, H. Shen, M. Wraback, B. Moody, H. S. Craft, R. Schlesser, R. F. Dalmau, and Z. Sitar, "Optically pumped UV lasers grown on bulk AlN substrates," *physica status solidi (c)*, vol. 9, no. 3-4, 2012.

[48] H. Yoshida, Y. Yamashita, M. Kuwabara, and H. Kan, "A 342-nm ultraviolet AlGaN multiple-quantum-well laser diode," *Nature Photonics*, vol. 2, no. 9, pp. 551–554, 2008.

[49] W. W. Chow and M. Kneissl, "Laser gain properties of AlGaN quantum wells," *Journal of Applied Physics*, vol. 98, no. 11, p. 114502, 2005.

[50] T.-T. Kao, Y.-S. Liu, M. M. Satter, X.-H. Li, Z. Lochner, P. D. Yoder, T. Detchprohm, R. Dupuis, S.-C. Shen, J.-H. Ryou, Y. Wei, H. Xie, A. Fischer, and F. A. Ponce, "Sub–250 nm, Low–Threshold Deep–Ultraviolet AlGaN–based Heterostructure Laser Employing HfO_2/SiO_2 Dielectric Mirrors," *Accepted for Appl. Phys. Lett.*, 2013.

[51] T. Katsuno, Y. Liu, D. Li, H. Miyake, K. Hiramatsu, T. Shibata, and M. Tanaka, "n-type conductivity control of AlGaN with high Al mole fraction," *physica status solidi (c)*, vol. 3, no. 6, pp. 1435–1438, 2006.

[52] M. L. Nakarmi, K. H. Kim, K. Zhu, J. Y. Lin, and H. X. Jiang, "Transport properties of highly conductive n-type Al-rich $Al_xGa_{1-x}N$ ($x \geq 0.7$)," *Applied Physics Letters*, vol. 85, no. 17, pp. 3769–3771, 2004.

[53] B. Cheng, S. Choi, J. E. Northrup, Z. Yang, C. Knollenberg, M. Teepe, T. Wunderer, C. L. Chua, and N. M. Johnson, "Enhanced vertical and lateral hole transport in high aluminum-containing algan for deep ultraviolet light emitters," *Applied Physics Letters*, vol. 102, no. 23, p. 231106, 2013.

[54] Z. Lochner, T.-T. Kao, Y.-S. Liu, X.-H. Li, M. M. Satter, S.-C. Shen, P. D. Yoder, J.-H. Ryou, R. D. Dupuis, Y. Wei, H. Xie, A. Fischer, and F. A. Ponce, "Room-temperature optically pumped algan-aln multiple-quantum-well lasers operating at <260nm grown by metalorganic chemical vapor deposition," 2013.

[55] Z. Lochner, T.-T. Kao, Y.-S. Liu, X.-H. Li, M. M. Satter, S.-C. Shen, P. D. Yoder, J.-H. Ryou, R. D. Dupuis, Y. Wei, H. Xie, A. Fischer, and F. A. Ponce, "Deep-ultraviolet lasing at 243 nm from photo-pumped AlGaN/AlN heterostructure on AlN substrate," *Applied Physics Letters*, vol. 102, no. 10, p. 101110, 2013.